



## Article

# Simplified Analytical Methods for Prefabricated Concrete Wall Panel Building System with Alveolar-Type Joints

Yang Xiao <sup>1</sup>, Xiaoyong Luo <sup>1,2</sup> , Minliang Xing <sup>1,\*</sup>, Zhen Pan <sup>1</sup>, Junfeng Cheng <sup>1</sup>  and Jinhong Liu <sup>1</sup>

<sup>1</sup> School of Civil Engineering, Central South University, Changsha 410075, China; csuxiaoyang@126.com (Y.X.); csu-luoxiyong@csu.edu.cn (X.L.)

<sup>2</sup> Engineering Technology Research Center for Prefabricated Construction Industrialization of Hunan Province, Changsha 410075, China

\* Correspondence: xml13140326@163.com

**Abstract:** This paper presents a type of prefabricated concrete wall panel building system with novel flexible alveolar-type joints, which has the advantages of fast assembly and controllable quality. Seven alveolar-type joint specimens were designed and fabricated to investigate the influence of the axial compression ratio, the size of the joint (in the interface contact area), and the strength of the mortar on the joints' performance. The shear-slip constitutive model of the alveolar-type joints was established on this basis. The accuracy of the constitutive model was verified by comparing two full-scale loading tests with the exact finite element analysis model of ABAQUS. A finite element model of a multi-story apartment building was established by using the aforementioned shear-slip constitutive model; thus, the simplified analysis method for the prefabricated concrete wall panel building structure with alveolar-type joints was proposed. It was concluded that increasing the axial compression ratio, mortar strength, and size of the joints could increase the shear-bearing capacity by different degrees and that the 50 mm depth joint could increase the capacity by 18.6%. The proposed shear-slip constitutive model simulated the interface mechanism well by comparing the test results. Furthermore, the simplified analytical methods of the integral structure were in good agreement with the FEA results.

**Keywords:** alveolar-type joint; PC wall panel; interface analysis; finite element analysis; simplified analytical methods



**Citation:** Xiao, Y.; Luo, X.; Xing, M.; Pan, Z.; Cheng, J.; Liu, J. Simplified Analytical Methods for Prefabricated Concrete Wall Panel Building System with Alveolar-Type Joints. *Buildings* **2023**, *13*, 1177. <https://doi.org/10.3390/buildings13051177>

Academic Editor: André Furtado

Received: 2 April 2023

Revised: 25 April 2023

Accepted: 26 April 2023

Published: 28 April 2023



**Copyright:** © 2023 by the authors. Licensee MDPI, Basel, Switzerland. This article is an open access article distributed under the terms and conditions of the Creative Commons Attribution (CC BY) license (<https://creativecommons.org/licenses/by/4.0/>).

## 1. Introduction

In recent years, precast construction technology has increased progressively and has been employed in a variety of structural applications. Prefabricated concrete wall panel building has become one of the most important developments in housing construction because of its sustainable development advantages, such as how it reduces formwork demand, saves on labor costs, and its quality control [1,2]. Prefabricated concrete wall panel building is a precast concrete construction technology that adopts factory precast concrete wall panel members as the main bearing members, which are connected into an integral whole through the on-site assembly. This technology is being further developed for low- and multi-story buildings across Europe and in countries such as Australia, Japan, and China [3,4].

Unlike cast-in-situ structures, the connection behaviors of prefabricated concrete wall panels are regarded as one of the most crucial factors affecting the seismic performance and integrity of structures built using this technology. Scholars have conducted numerous studies on these joint connections in PC structures, including the following methods: lap splicing longitudinal bars using sleeves, unbonded post-tensioned connections, bolt connections, and sitting slurry connections with non-connected reinforcement. Mochizuki and Bhatt [5,6] discussed the effects of vertical and horizontal joints on the seismic performance

of the PC structures. They showed that different tectonic forms of 312 horizontal and vertical joints had significant impacts on seismic performance. Ling et al. [7–9] discussed the factors that influence the seismic performance of PC structures—such as the diameter of steel bars, the lapped length of rebars, and the arrangement mode (single and double rows) of grouted sleeves—and proposed reasonable suggestions. Zhou et al. [10] proposed an innovative steel sleeve and box connection, based on the pulled-out and shear tests. The effects of their design parameters were determined by finite element analysis to improve the connections. Yahya [11] and Robin [12] studied the shear and seismic performance of unbonded and post-tensioned structures, respectively. These studies helped to put forward the corresponding design calculation methods. Their results showed that tensioned prestressed wall structures have a good connection performance. However, although these structures showed a better connection performance, there are still many problems in their practical application: high installation accuracy requirements, grouting and anchored quality cannot be guaranteed, and the construction cost is difficult to control. Therefore, to solve the fabrication problems of PC walls, which were caused by too many connection joints, Xiao et al. [13] proposed a novel PC shear wall structure with unconnected, vertically distributed reinforcement. Furthermore, they also increased the longitudinal reinforcement in the boundary elements by using the equal capacity design method with cast-in-place shear walls, which provided a new idea for connections in PC shear walls.

In addition, with the advancement and development of technology in this field, more PC wall panel building methods are also being developed. The large prefabricated plate structures, which were widely used at the end of the last century, had the advantages of fast construction speeds and high degrees of industrialization. However, some obvious defects in these structures have since been found. For example, they are waterproof and impermeable and have issues with thermal and sound insulation. These shortcomings have not yet been improved [14]. German scholars have proposed a new structure that is similar to sandwich-prefabricated, superimposed RC wall panels, which replaced the traditional template casting with a combination of factory prefabrication and casting-in-place [15–17]. Zhang et al. [18] found that the deformation of prefabricated parts and cast-in-place parts in these composite wall panels were synchronous using a low-cycle reciprocating test and a simulation analysis. The composite surface was found to achieve better common work and good mechanical performance; however, plenty of wet work was still necessary, leading to a chaotic on-site environment. In addition, in order to reduce the weight of these PC wall panels, a type of prefabricated, hollow-core wall panel was developed, which can be used as a non-load-bearing wall. However, if the core of such is filled, it can also be used as a load-bearing wall [19]. Many scholars [20–23] have conducted relevant research in this regard and have found that although hollow-core RC walls have good ductility and energy dissipation capacities, the bearing capacity of these wall panels in seismic activity and compression is poor.

Considering the shortcomings of the aforementioned connections and the prefabricated wall panel systems, in this paper, we propose a new, assembled, integral wall panel building system with flexible alveolar-type joints [2]. This system was based on the principle of mortise and tenon in traditional wooden structures and can be applied to both low-rise or multi-story residential buildings, as shown in Figure 1a. In this system, the horizontal joint adopts a seat slurry connection, and the prefabricated floor slab is connected with the upper and lower prefabricated wall panels through the bottom convex teeth and the upper groove, respectively, as shown in Figure 1b. Figure 1c shows the vertical joint, where it can be seen that polyethylene (PE) or polyurethane (PU) bars are first used to seal the joint opening and are then used for mortar grouting. This novel-connection wall panel building structure system has the following advantages: (1) The alveolar-type form of the joints increases the interface contact area, which helps to improve the shear-bearing capacity and strengthen the lateral stiffness of the wall panels. (2) Its three waterproof structures also help to prevent water from entering from the external wall to the internal wall. (3) It provides stability by relying on the self-weight of the panels and can help to limit

the position in the installation of the wall panels so as to improve the fault tolerance rate, which saves time in the construction site assembly. However, although it has advantages, there are still many problems to be solved before this can be applied to engineering.

Consequently, seven alveolar-type joint specimens were designed and constructed, and monotonic loading tests were conducted on these specimens to investigate the shear-slip constitutive model of the novel joint [10]. Furthermore, the finite element model was established by using the ABAQUS program on the basis of a full-size-specimen pseudo-static test, to verify the accuracy of the above constitutive model. Finally, the integral FEA model was constructed based on a multi-story building, which helped us propose the simplified analytical method for the prefabricated concrete wall panel buildings [24] with alveolar-type joints. The calculated results were in good agreement with the FEA results, which were obtained through an example analysis.

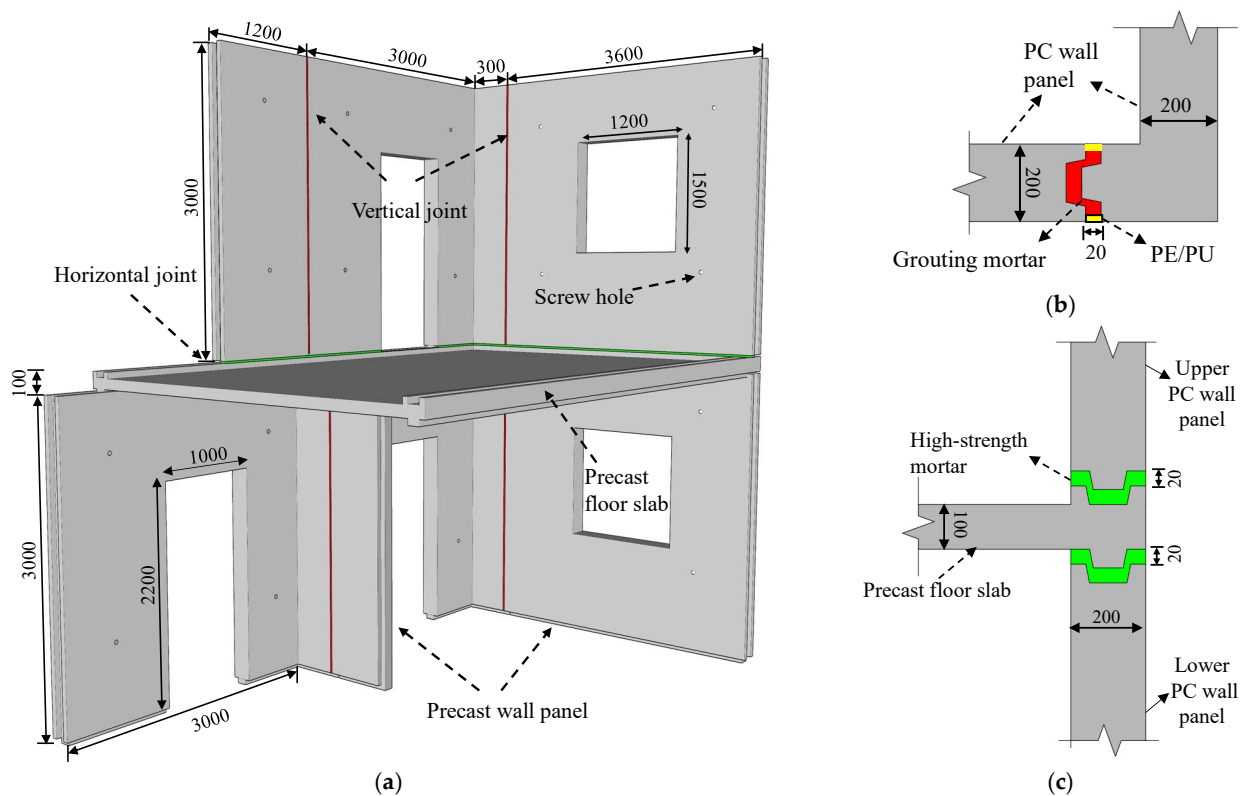


**Figure 1.** Prefabricated concrete wall panel building (unit: mm), (a) joint of alveolar-type wall panel; (b) vertical joint; and (c) horizontal joint.

## 2. Constitutive Model of Alveolar-Type Joints

### 2.1. Experiment Study

#### 2.1.1. Experimental Preparation

Seven PC wall panel specimens with alveolar-type joints were designed and constructed. Each specimen was composed of an upper wall panel, a bottom base, and an alveolar-type horizontal joint. This was similar to the PC wall panel structure proposed in [10,25,26]. They were labeled as CW1–CW7. The main design parameters for our specimens were the joint size (interface contact area), the axial compression ratio, and the strength of the mortar. The thickness of the wall panels was 200 mm. The length of CW1–CW3 was 800 mm, and the alveolar-type joint depth was chosen as 0 mm, 20 mm, and 50 mm, respectively, as shown in Figure 2. The axial compression ratio was 0.1 and the joint mortar was a high-strength material with a nominal strength of 50 MPa. Conversely, the length of CW5–CW7 was 600 mm, with a 50 mm alveolar-type depth, and the axial compression ratio was controlled as 0, 0.1, and 0.2 [2], respectively. The cement mortar

was used as a normal material, for which the design strength was 30 MPa. Furthermore, CW4 was controlled at 0.1 axial compression ratio, 800 mm wall length, and 30 MPa design strength of the joint mortar. The main design parameters of the specimens are listed in Table 1. The total height of each specimen was 870 mm, including the grout layer thickness of 20 mm, the height of the upper wall panel was 350 mm, and the lower wall panel extended 100 mm. The size of the bottom base was 1500 mm × 600 mm × 400 mm. The reinforcement diagram of the specimen and the relevant size diagram are shown in Figure 2. Moreover, the precast members were cast from the same C30 grade concrete and the reinforcement type was HRB400. According to the material performance test [27], the cube compressive strengths of concrete, high-strength mortar, and normal mortar, at a curing time of 28 days, were 36.9 MPa, 50.5 MPa, and 32.3 MPa, respectively.

**Table 1.** Main parameters of specimens.

Specimen No.	Depth of Alveolar-Type Joint	Interface Contact Area, $A_k$	Axial Compression Ratio	Vertical Loading	Strength of Mortar $f_{c,p}$
	(mm)	(mm <sup>2</sup> )	$l$	(kN)	(MPa)
CW1	0	800 × 200	0.1	228.8	50
CW2	20	800 × 232	0.1	228.8	50
CW3	50	800 × 282	0.1	228.8	50
CW4	50	800 × 282	0.1	228.8	30
CW5	50	600 × 282	0	0	30
CW6	50	600 × 282	0.1	171.6	30
CW7	50	600 × 282	0.2	343.2	30

Notes: the interface contact area of alveolar-type joints,  $A_k = l_c \times l_b$ , for  $l_c$  is the length of wall panel, and for  $l_b$  is the length of lower interface of alveolar-type joint—the red line in Figure 2b–d.

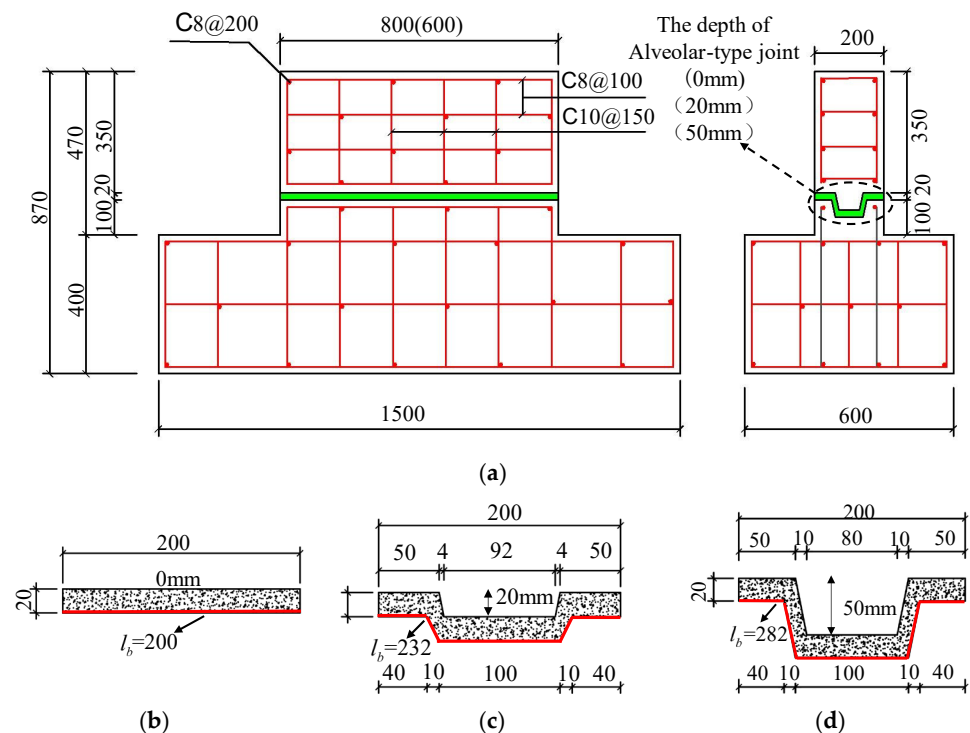


**Figure 2.** Geometric sizes and layout of reinforcing bars for specimens (unit: mm): (a) geometric sizes of specimens; (b) general joint; (c) 20 mm alveolar-type joint; and (d) 50 mm alveolar-type joint.

### 2.1.2. Test Setup and Loading History

To simulate the boundary and deformation conditions of the possible specimens, the multi-functional array loading test and analysis system were adopted, as shown in Figure 3a. Each specimen was fixed on the L-shaped foundation using anchor bolts and steel plates to prevent sliding. The lateral load and constant vertical load were applied at the lateral side and at the top of the wall panels, respectively, in accordance with the requirements of the Chinese code JGJ/T 101-2015 [28]. In addition, there was a force-sensor-sandwiched reaction beam and lifting jack to adjust axial compression, and displacement sensors were adopted to measure the slippage between the upper and lower wall panels [26]. A photograph of the loading setup is shown in Figure 3b. The vertical load was first applied to the predetermined value and then kept constant by monitoring the force sensor on the jack. Second, the horizontal load was applied by the actuator. In this case, force control was adopted before initial cracks occurred in the specimen, the increment of force loads at each stage was 5 kN. The displacement load control was conducted after initial cracks appeared, the increment for the displacement load of each stage was 0.2 mm, until the slippage reached 5 mm, or the lateral load had no obvious change. After this, the test stopped.

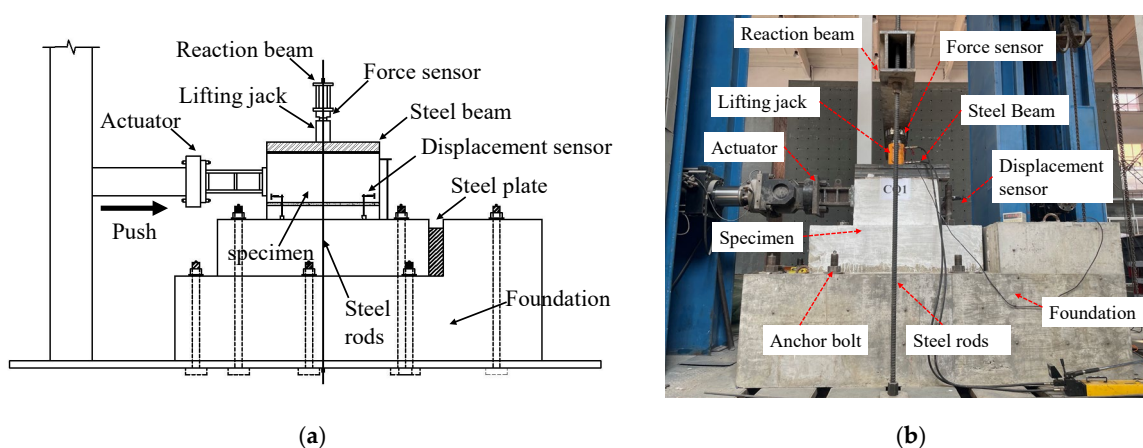


**Figure 3.** Schematic diagram of the loading device for specimens: (a) schematic diagram of the loading devices; and (b) a photograph of the devices.

### 2.1.3. Failure Model and Mechanism of Typical Specimens

The specimens showed different failure models under the conditions of axial compression and no axial compression, as depicted in Figure 4. The initial tiny cracks first appeared on the bottom section of the CW3 (0.1 axial compression ratio) during the early loading stage, as shown in Figure 4a. After this, the cracks extended along the mortar interface, when diagonal cracks were formed and concrete spalled. Finally, the cracks broke through. Conversely, although the initial cracks in CW5 (0 axial compression ratio) first began to occur at the loading area, they extended along the mortar interface quickly and there was no diagonal crack, as shown in Figure 4b.

Figure 4c describes the shear resistance mechanism of the alveolar-type joint interface. It can be seen that the horizontal load,  $P$ , was mostly balanced by two forces, interlock action (consisting of mechanical interlock and adhesive bonding) and shear friction under the constant vertical load [29,30]. At the beginning of the loading, there was no slippage at the interface, meaning that only interlock action existed. However, the shear friction began when the cracks appeared, and the interlock action decreased gradually. In the end, there was only shear friction due to the slip plane that was formed. However, the principal tensile stress (marked A in Figure 4d) of CW3 (which was under the constant vertical load) was oblique and caused diagonal cracks. This was different from CW5 (without vertical load)  $\sigma_y = 0$ , as there was only shear stress on the Mole element, which eventually caused shear failure mode.

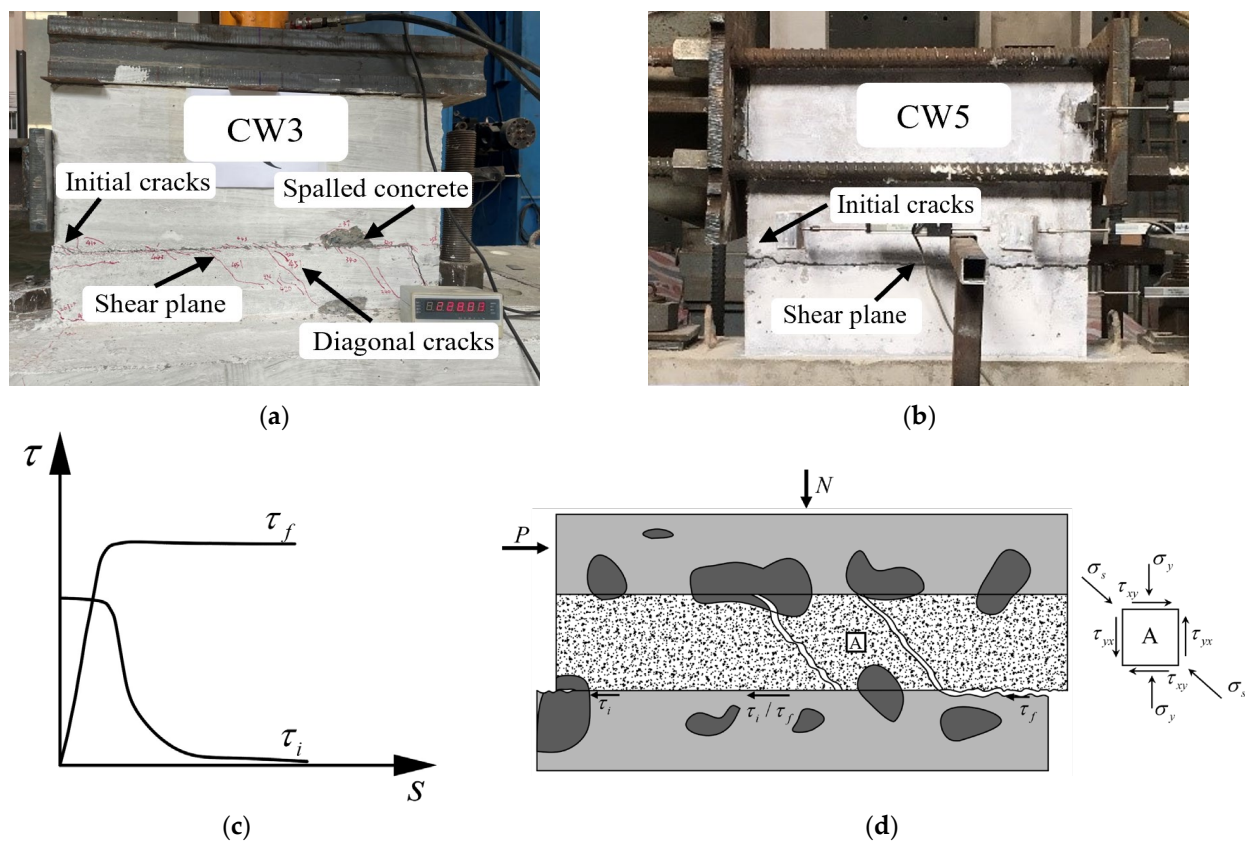


**Figure 4.** Failure models and mechanisms of typical specimens: (a) CW3, (b) CW5, (c) development of resistant forces, and (d) shear resistance mechanism of alveolar-type joint.

#### 2.1.4. Results and Discussion

Figure 5 depicts the force–slippage curves of CW1–CW7, which were measured directly through the force and displacement sensors on the wall panels. It was observed that curves can be described through approximately four stages. In the first stage, the slippage was basically zero with the increase in the loading because the interface had an initial shear resistance capacity. Cracks appeared as the loading continued to increase, and the load reached its peak in the second stage. Next, the initial slip surface was formed, and the load dropped sharply in the third stage. The final sliding plane was then formed and there was obviously misalignment between the upper and lower wall panels, which took the loads that tended to be stable.

It can also be seen in Figure 5a that the bearing capacity of CW1–CW3 increased successively with the increase in the depth of the alveolar-type joints. It should be noted that compared with CW1, the bearing capacity of CW2 and CW3 increased by 5.6% and 18.6%, respectively. This indicated that changing the depth of the joint can improve the bearing capacity to some extent. Furthermore, we found that the peak load of CW3 was 65.9% higher than that of CW4 due to the improvement of the mortar strength. As shown in Figure 5b, the axial compression ratios of CW5~CW7 were 0, 0.1, and 0.2, respectively, and the peak loads were 43.9 kN, 240 kN, and 385 kN, respectively. The peak load increased 5.5 times and 8.8 times, indicating that axial compression has a great influence on the joint-bearing capacity. Furthermore, the peak load of CW4 was higher than that of CW6 due to the longer wall panel length. Based on these findings, we concluded that, among the parameters affecting joint-bearing capacity, axial compression had the greatest influence, followed by mortar strength. The joint size had the least influence.

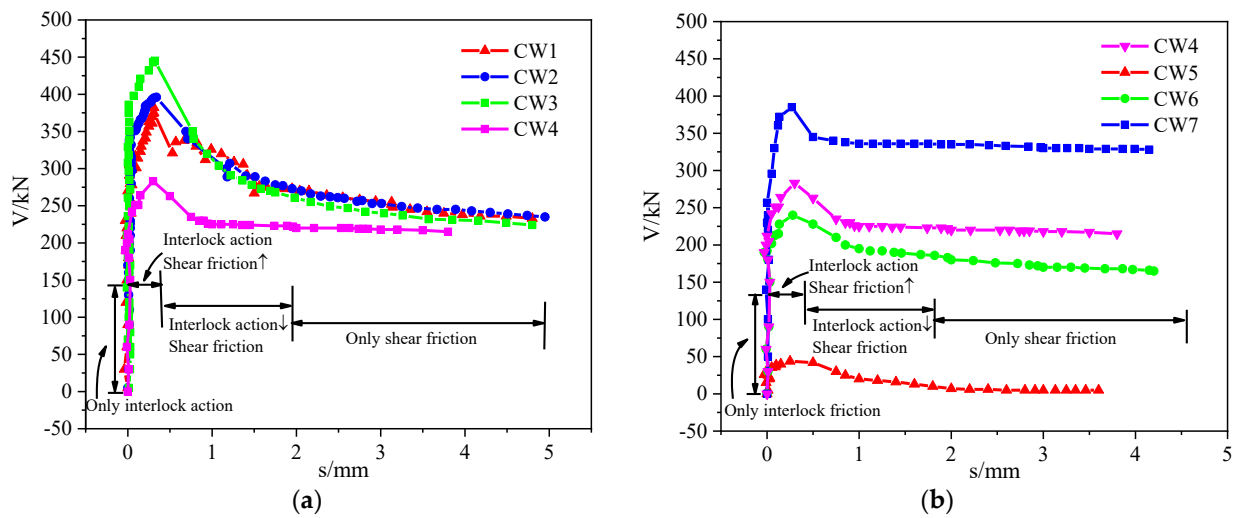


**Figure 5.** Force-displacement curves of CW1–CW7: (a) CW1–CW4 and (b) CW4–CW7.

## 2.2. Constitutive Model

### 2.2.1. Comparison of Different Methods of Shear Capacity

From the results of the tests that we performed on the specimens, we concluded that the shear resistance of the alveolar-type joint can be attributed to the shear properties of the joint surfaces in concrete and mortar. There are different methods that can be used to calculate shear strength: GB51231 T-2016 [31] specifies the shear strength of shear walls, and model code 2010 [32] specifies the ultimate shear strength at the joint interface of the assembled structures as a function of the adhesive bond, shear friction, and dowel action. Mattock and Hawkins [33] conducted an experimental study on 66 direct shear members of reinforced concrete in 10 groups and proposed the shear transfer formula, which considered the influence of factors such as reinforcement ratio and axial compression (which is more universal). Zhao Yong [34,35] proposed the grouting sleeve interface shear model on the basis of the study on the shear joint surfaces of new and old concrete with high strength. They took into account the contribution of the adhesive locking action, pin action, and shear friction action to the shear capacity. The shear capacity model formulas are as follows:

$$\tau_{u,JGJ} = 0.6\rho f_y + 0.8\sigma_n \quad (1)$$

$$\tau_{u,MC} = c_a \cdot f_{ct} + \mu\sigma_n \leq 0.5\nu f_c \quad (2)$$

$$\tau_{u,Mattock} = 0.467f_c^{0.545} + 0.8(\rho f_y + \sigma_n) \quad (3)$$

$$\tau_{u,zhao} = \alpha_c f_c + \alpha_f \rho f_y + \alpha_d \rho \sqrt{f_c f_y} \quad (4)$$

where  $\tau_u$  is the shear resistance stress;  $\rho$  is the rebar ratio crossing the joint interface;  $\rho = 0$  due to no reinforcement on the joint;  $f_y$  is the yield strength of steel reinforcement in tension;  $\sigma_n$  is the is the compressive stress resulting from a normal force acting on the interface;  $c_a$  is the coefficient for the adhesive bond, which depends on the roughness of the interface;  $f_{ct}$  is the design value of the axial tensile strength of concrete, which can be calculated by  $f_t = 0.375f_c^{0.55}$ ;  $\mu$  is the friction coefficient, which also depends on the roughness of the interface;  $\nu$  is the reduction factor for the strength of the diagonal concrete strut,  $\nu = 0.55 \cdot (30/f_c)^{1/3} \leq 0.55$ ;  $f_c$  is the axial compressive strength of concrete, which can be calculated by  $f_c = 0.76f_{cu}$ , in which  $f_{cu}$  is the measured compressive strength of a 150 mm-cube concrete specimen;  $\alpha_c$  is the combination coefficient of the adhesion action;

$\alpha_f$  is the combination coefficient of the frictional shear action; and  $\alpha_d$  is the combination coefficient of the reinforcement pin action. The corresponding coefficients were defined as  $\alpha_a = 0.5$ ,  $\mu = 1.0$ , and  $\alpha_c = 0.025$  for a very rough interface [32,34].

### 2.2.2. Modified Shear Capacity Method

The shear resistance capacity of CW1–CW7 was calculated by Equations (1)–(4). Figure 6 compares the specimens' peak loads, as determined by the test results and the formula values. The results of Equation (1) were lower than the test, which ignored the interlock action. The results of Equations (2) and (3) were higher than the test because rebars can improve the initial adhesion and interlock action of the interface. Furthermore, the results calculated using Equation (4), which did not consider compressive stress, were generally lower than the test values. As a result, based on the parameter analysis, Equations (6) (below) was proposed to modify the shear resistance capacity of the alveolar-type joints.

$$\tau_u = \alpha_c K f_c + \mu \sigma_n \quad (5)$$

$$V_u = \tau_u A_c \quad (6)$$

where  $\alpha_c$  is the combination coefficient of the adhesion action (positively correlated with the mortar strength), which was directly taken as 0.03 for the high-strength mortar and as 0.01 for the normal mortar [34];  $K$  is the joint dimension effect coefficient,  $K = A_k / A_c$ , for which the values were 1, 1.16, and 1.41, and the depth of the alveolar-type joint is 0 mm, 20 mm, and 50 mm;  $\mu$  was taken as 1.0, and there was a 6 mm-deep pitch rough surface, as followed in Model code 2010 [32].

Table 2 compares the results of the test and the modified method, showing that their deviation was within 10%. It can be concluded that the modified shear resistance capacity method agrees well with the test results.

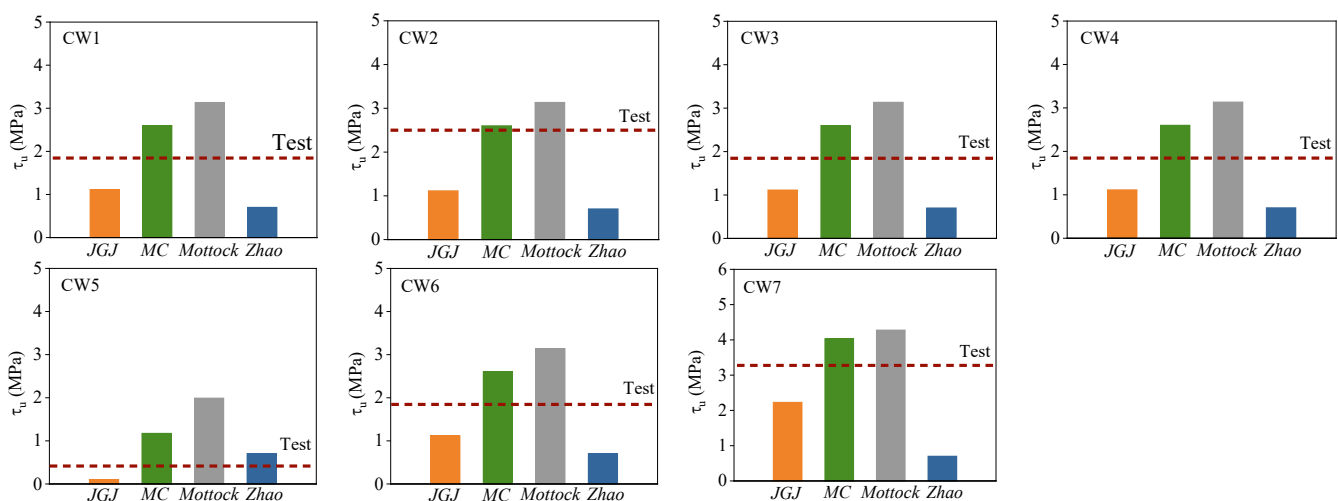


**Figure 6.** Comparison between the test and formula results of CW1–CW7's peak loads.

### 2.2.3. Shear–Slip Constitutive Model

As mentioned above, the force–displacement curves present the four stages at the alveolar-type joint interface. Table 3 collects the turning characteristic points of each stage, including the cracking load, peak load, sudden drop load, and the final load. It is worth noting that the cracking load was positively correlated with the peak load, while the sudden drop load and final load were mainly related to axial compression. In order to summarize the law, the cracking load is normalized according to the peak load, and the sudden drop load and final load are calculated by the friction action, just as Equation (7) shows. Figure 7 presents the constitutive model of the alveolar-type joint interface after using broken lines



and characteristic points. Figure 8 shows the test results and the constitutive model values calculated using Equations (5)–(7). It can be seen here that there were some differences between the two sets of results, which can be described by the general trend of force change with slippage at the interface of the alveolar-type joints.

**Table 2.** Comparison of the modified method and test results.

Specimens	$\alpha_c$ /	$K$ /	$\sigma_n$ MPa	$\tau_u$ MPa	$A_c$ mm <sup>2</sup>	$V_{u,M}$ kN	$V_{u,T}$ kN	Deviation /
CW1	0.03	1.00	1.43	2.271	800 × 200	363.4	382	4.87%
CW2	0.03	1.16	1.43	2.406	800 × 200	384.9	396	2.80%
CW3	0.03	1.41	1.43	2.616	800 × 200	418.6	445	5.94%
CW4	0.01	1.41	1.43	1.825	800 × 200	292.1	283	3.09%
CW5	0.01	1.41	0	0.395	600 × 200	47.4	44	8.07%
CW6	0.01	1.41	1.43	1.825	600 × 200	219.0	240	8.73%
CW7	0.01	1.41	2.86	3.255	600 × 200	390.6	385	1.47%

Note:  $V_{u,M}$  is the value calculated by modified method and  $V_{u,T}$  is the test result.

**Table 3.** Characteristic test points of specimens.

Specimens	$V_c$ kN	$s_c$ mm	$V_u$ kN	$s_u$ mm	$V_d$ kN	$s_d$ /mm	$V_l$ kN	$s_l$ mm
CW1	357	0	382	0.31	270	2.04	233	4.80
CW2	351	0	396	0.34	245	2.17	235	4.95
CW3	386	0	445	0.32	249	2.20	224	4.80
CW4	212	0	283	0.30	220	1.86	200	3.80
CW5	30	0	44	0.25	7	2.00	5.00	3.60
CW6	192	0	240	0.28	180	1.95	165	4.20
CW7	256	0	385	0.27	335	2.01	328	4.15

Note:  $V_c$  is the crack load;  $s_c$  is the corresponding slippage of  $V_c$ ;  $V_u$  is the peak load;  $s_u$  is the corresponding slippage of  $V_u$ ;  $V_d$  is the down load;  $s_d$  is the corresponding slippage of  $V_d$ ;  $V_l$  is the final load; and  $s_l$  is the corresponding slippage of  $V_l$ .

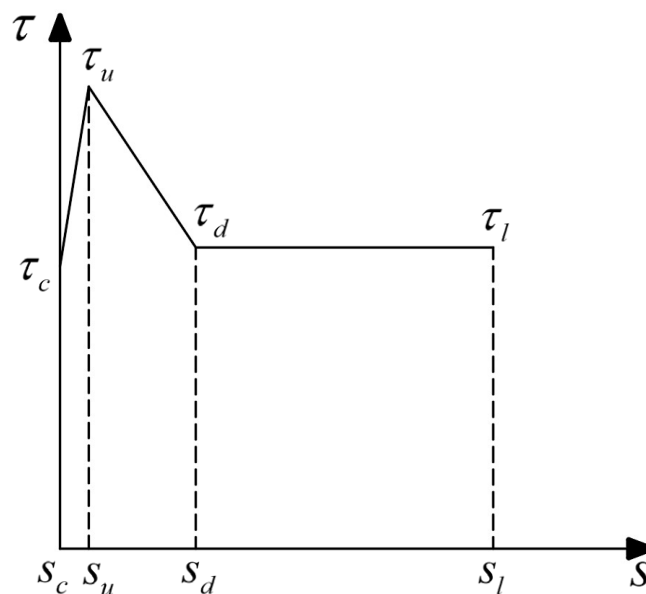


**Figure 7.** Constitutive model of the alveolar-type joints.

$$\begin{cases} \tau_c = 0.8\tau_u & s_c = 0 \text{ mm} \\ \tau_u = \alpha_c K f_c + \mu \sigma_n & s_u = 0.3 \text{ mm} \\ \tau_d = \mu \sigma_n & s_d = 2 \text{ mm} \\ \tau_l = \tau_d & s_l = 4 \text{ mm} \end{cases} \quad (7)$$

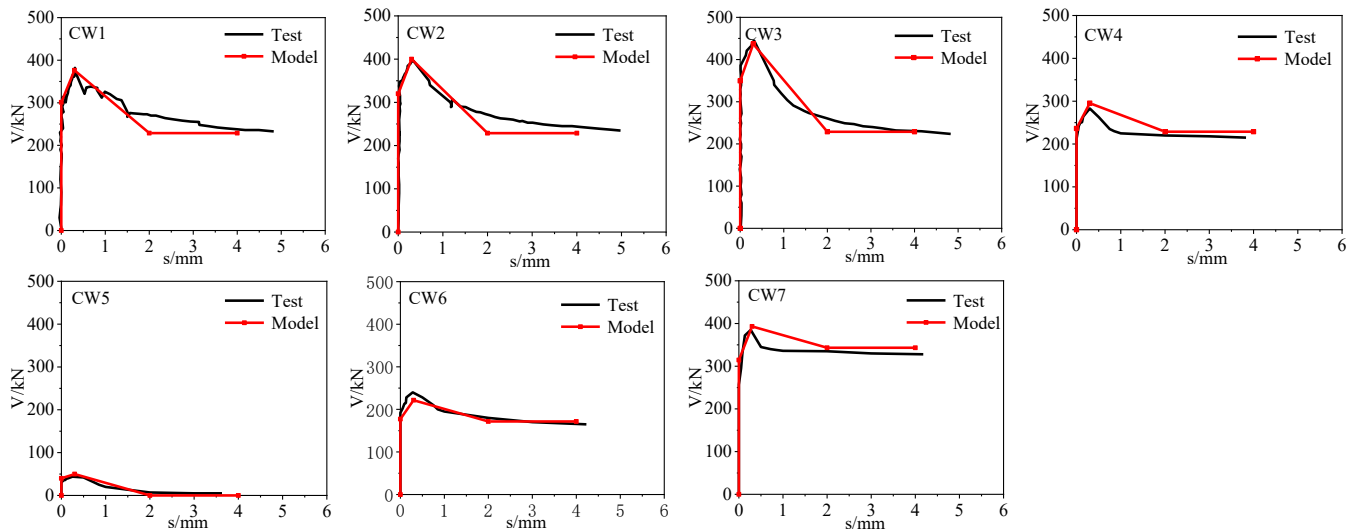


Figure 8. Comparison of the constitutive model and test results of specimens.

### 3. Finite Element Analysis and Verification

#### 3.1. Full-Scale Wall Panel Loading Test

Two full-scale, precast wall panel specimens with alveolar-type joints were designed and constructed in this study. They were tabled as PW1 and PW2. Each specimen consisted of an upper concrete wall with hidden columns on both sides; a bottom beam; and alveolar-type joints with depths of 50 mm. PW1, the upper prefabricated wall, was the whole wall panel, and PW2 consisted of the left and right wall panels, which were connected through vertical joints and had the same structure as the horizontal joints. In addition, the designed strength grade of the concrete was C30, whereas the designed strength grade of the mortar was 50 MPa and the steel reinforcement label was HRB400. Figure 9 shows the dimensions of the specimens (taking PW2 as an example). The dimensions of the upper wall panel were 3000 mm × 2000 mm × 200 mm, the size of the bottom beam was 2500 mm × 1300 mm × 500 mm, and the width of the hidden column was 300 mm. A photograph was taken to show the loading setup in Figure 10 (taking PW2 as an example). Anchor bolts were used to fix the base to the ground and jacks were set on both sides to fix the base again to prevent slippage in the loading process. Steel beams were arranged outside the plane of the wall panel to prevent out-of-plane instability in the loading process. The vertical actuator evenly distributed the vertical load to the whole wall by loading the steel beam, and the lateral load was applied at the lateral side of the wall, which had a height of 2800 mm. The lateral displacement on the right side of the specimens was recorded by the displacement sensors. According to JGJ/T101-2015 Building Seismic Test Regulations [28], the force–displacement hybrid loading mechanism was adopted for the specimens during the test. In this case, force control was adopted before the specimen showed cracks, and the load increment of each grade was either 5 kN or 10 kN. The test switched to displacement load control after cracking occurred, and the increments for the displacement load of each stage reached a cracked displacement. The loading ended when the lateral load dropped below 85% of the peak load [2].

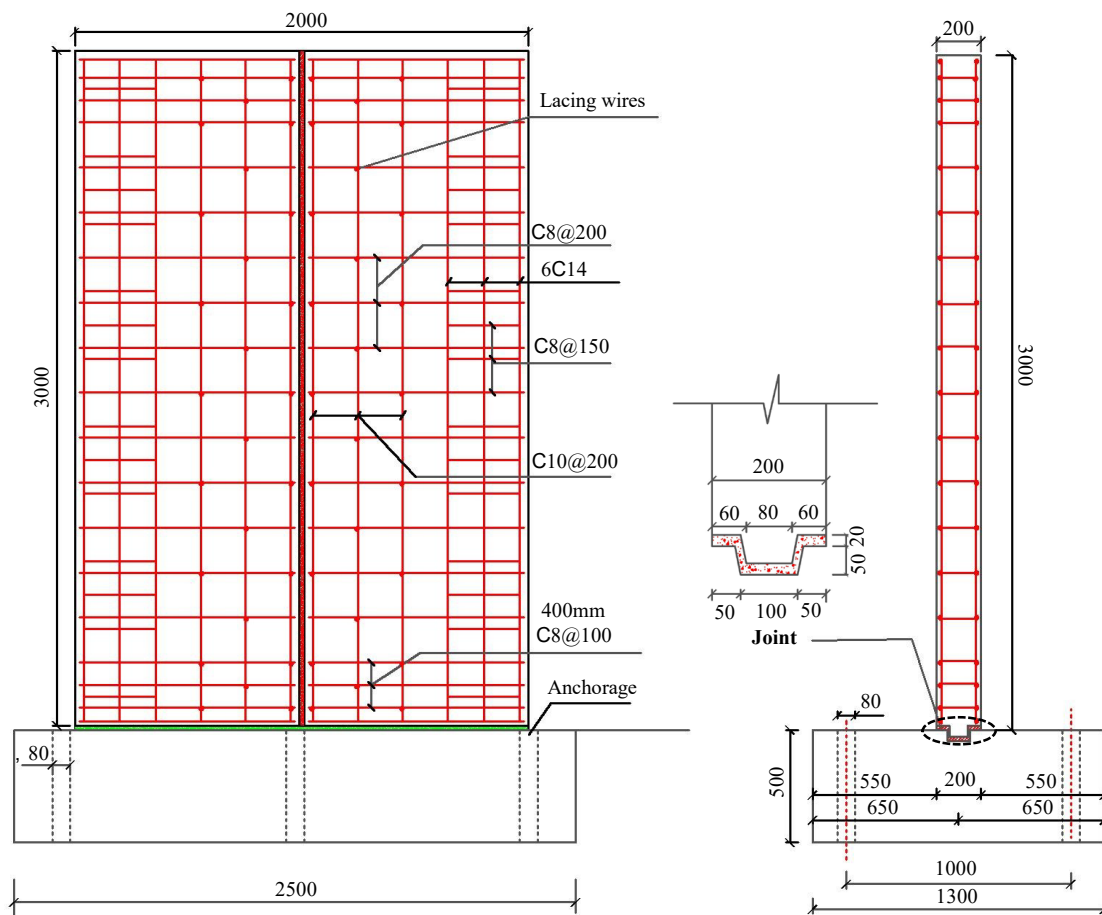


Figure 9. Geometric sizes and layout of reinforcing bars of PW2 (unit: mm).

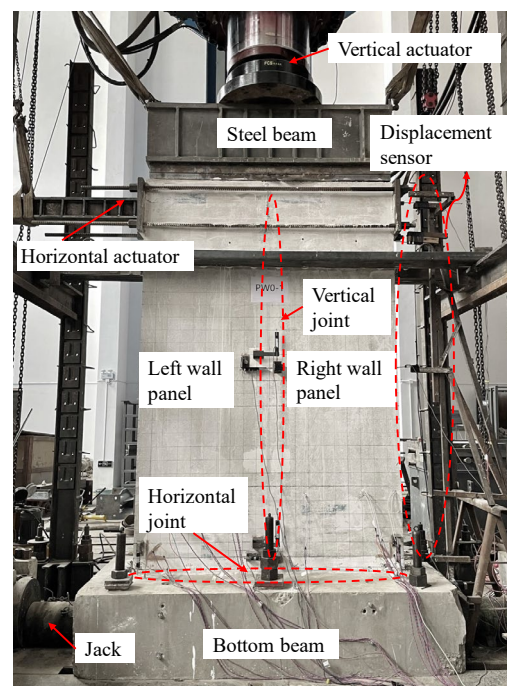


Figure 10. A photograph of pseudo-static test setup.

### 3.2. FEA of Full-Scale Wall Panel

#### 3.2.1. Element Types and Loading Steps

For the finite element analysis (FEA), the PC wall panel model was established using the separation model in ABAQUS. All parts were modeled by eight-node solid elements with reduced integration (C3D8R) after creating partitions except for the steel reinforcement, which used the two-node truss element (T3D2) [15,36–42]. It should be noted that all reinforcements are modeled as a perfect bond with concrete in the model, whereas, in the ABAQUS program the reinforcement was “embedded” in the concrete [36,40,42,43]. At the same time, to address the accuracy and efficiency of the calculations, the mesh size of 50 and 100 mm was adopted for the upper wall panel and the bottom beam, respectively, and the size of the T3D2 elements simulating steel bars is 30 mm [36–39]. In order to improve convergence as well as achieve a higher accuracy of simulation, there was an independent additional node established to couple with the loading surface, so as to realize the synchronous displacement of the loading point and surface, as shown in Figure 11. Of note, all the degrees of freedom at the bottom of the foundation are constrained, as well as the out-of-plane displacement of the horizontal loading point. The non-linear problem was solved by the static general analysis method available in ABAQUS, which adopts a Complete Newtonian with high computational accuracy. Three analysis steps are set for the simulation. First, the constant axial load is applied at the reference point; then the horizontal displacement is sequentially applied at the reference point.

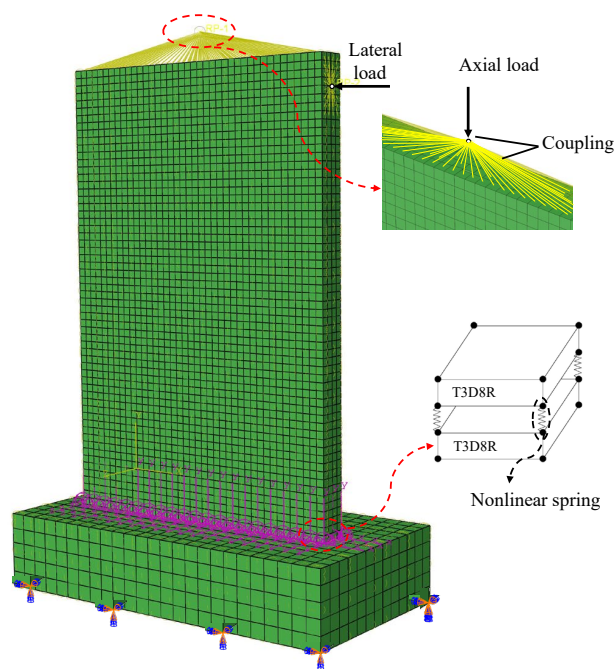
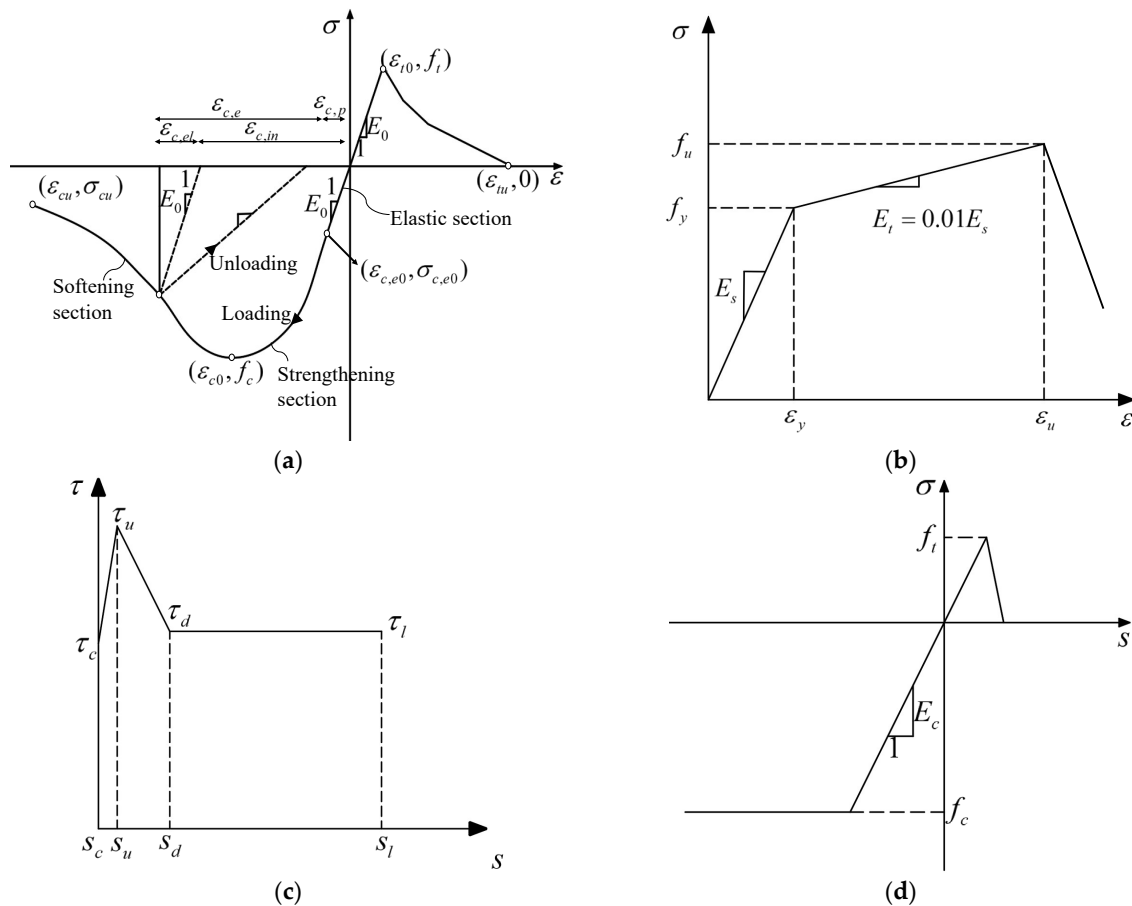


Figure 11. Model of FEA.

#### 3.2.2. Material Constitutive Model

Figure 12a shows the stress–strain relationship of concrete defined in GB50010-2010 [44], which was calculated using the damage plasticity model (CDP) in ABAQUS. It assumed that there was no associated potential flow rule and used the yield surface to illustrate the different evolution under tension and compression (Lubliner et al., 1989 [45]; Lee and Fenves, 1998 [46]). In the figure, it can be seen that the stress–strain relationship of the concrete under uniaxial compression was composed of an elastic section, a strengthening section, and a softening section. In addition,  $\varepsilon_{c,e0}$  denotes the elastic limit strain corresponding to  $\sigma_{c,e0}$ ;  $\varepsilon_{c0}$  denotes the peak concrete compressive strain corresponding to  $f_c$ ;  $f_t$  denotes the representative uniaxial tensile strength of the concrete; and  $\varepsilon_{t0}$  denotes the peak tensile strain of the concrete corresponding to  $f_t$ . The five plasticity parameters (dilation angle  $\varphi$ ,

flow potential eccentricity  $e$ , yield surface function  $f_{b0}/f_{c0}$ , shape factor  $K_c$ , and viscosity parameter ( $\lambda$ ) in the CDP model of the ABAQUS library were taken as 30, 0.1, 1.67, 0.667, and 0.005. The bilinear hardening model was adopted for the steel reinforcement, which presents linear elastic changes before yield and simplifies to a gentle oblique straight line after yield following the Von mises yield criterion and isotropic hardening,  $f_y$  denotes the yield strength of steel;  $\epsilon_y$  denotes the yield strain of steel corresponding to  $f_y$ ;  $f_u$  denotes the ultimate strength of steel; and  $\epsilon_u$  denotes the peak steel strain corresponding to  $f_u$ , as shown in Figure 12b. Table 4 presents the main parameters of the materials.



**Figure 12.** Constitutive relationship in FEA model: (a) uniaxial constitutive model for concrete; (b) bilinear hardening model for steel; (c) tangential constitutive at the interface; and (d) normal constitutive at the interface.

**Table 4.** Parameters of the materials.

Material	$\rho$	$E$	$\mu$	$f_c$	$f_y$
	kg/m <sup>3</sup>	MPa	/	MPa	MPa
Concrete	2400	31,843	0.2	28.04	-
Reinforcement	7850	$2.1 \times 10^5$	0.3	-	450

### 3.2.3. Contact Surface

A nonlinear spring-2 element was employed between the upper wall panels and bottom beam to simulate the slip behavior at the horizontal joints [10,47], shown in Figure 11. In order to verify the accuracy of the interface constitutive model, the tangential constitutive relation was based on the model shown in Figure 12c, for which the characteristic points were calculated according to Equation (8). Figure 12d shows the stress–strain relationship

at the joint interface utilized in the normal direction,  $f_c$  denotes the ultimate compressive strength of the concrete, and  $f_t$  denotes the ultimate tensile strength of the concrete in the figure. In addition, considering that cracks did not occur in the vertical joints during the test, in the simulation of vertical joints between the left and right wall panels, a hard contact was applied in the normal direction, which allows the two contact surfaces to separate from but not penetrate each other. Meanwhile, the Mohr–Coulomb friction model was used in the tangential direction, which applied the “penalty” contact in ABAQUS, and the friction coefficient was set as 1.0.

### 3.3. Comparison and Verification

Figure 13 shows the skeleton curve results between the FEA and the test of PW1 and PW2. It can be seen that the simulation results were in good agreement with the test results and that the difference between the two peak bearing capacities was less than 10%. Furthermore, the test results also showed that the wall stiffness in the early stage was larger, as the alveolar-type structure used in the test had a corresponding constraint effect on the joint position. With the increase in displacement, the bearing capacity of the test component decreased, while the calculation curve tended to be smooth due to the pseudo-static and single-direction loading modes that were adopted in the tests and the FEA.

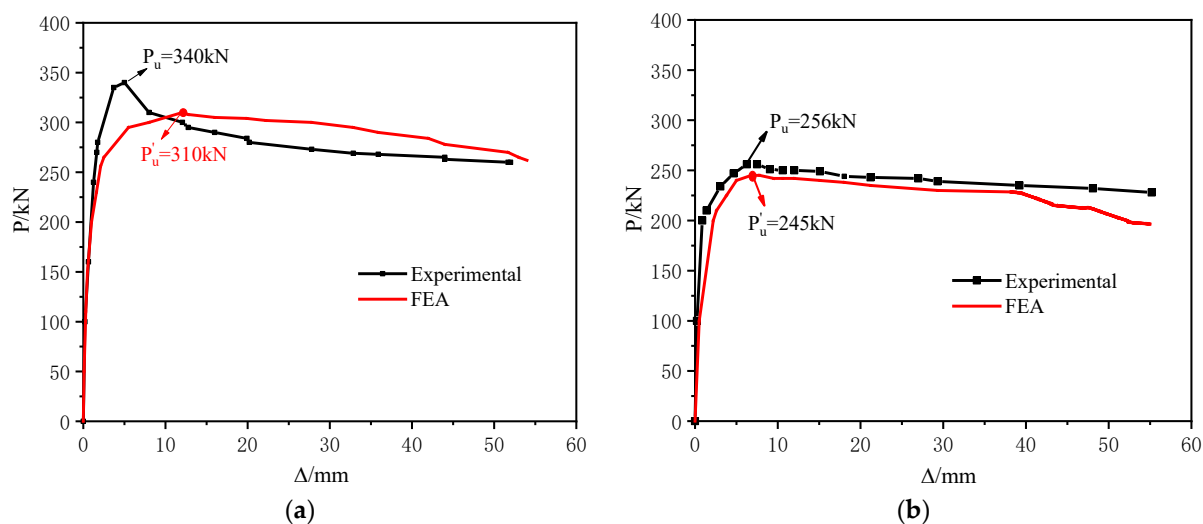


**Figure 13.** Load–displacement curves of the test and FEA: (a) PW1 and (b) PW2.

In addition, the results of the concrete compression damage under the final loading displacement of the model were extracted and compared with the results of the failure modes, as shown in Figures 14 and 15. According to Figures 14 and 15e, the damage to PW1 and PW2 was concentrated in the bottom horizontal alveolar-type joint, and in one side corner of the wall panel that was obviously raised up. This was consistent with the FEA results, in which the damage was concentrated in the bottom seam, as shown in Figures 14 and 15a–d. Compared with PW1, the bearing capacity of PW2 was lower because the left and right wall panels of PW2 were not continuous at the horizontal joints, which weakened the horizontal connections, and in this case, there was significant damage on the left wall panel. However, no cracks were generated in the vertical joint during the loading process, which corresponded to the FEA results, shown in Figure 14c. We concluded that, although the vertical joint had a weakening effect on the wall bearing capacity, it could still realize the cooperative work between the wall panels.

By comparing the results of the test and the FEA, it can be seen that the finite element model parameter setting and the interface constitutive model can effectively simulate the real environment of the wall panel structural system with horizontal and vertical alveolar-type joints. Therefore, on this basis, an overall model can be established to analyze the structure of the prefabricated wall panel system.

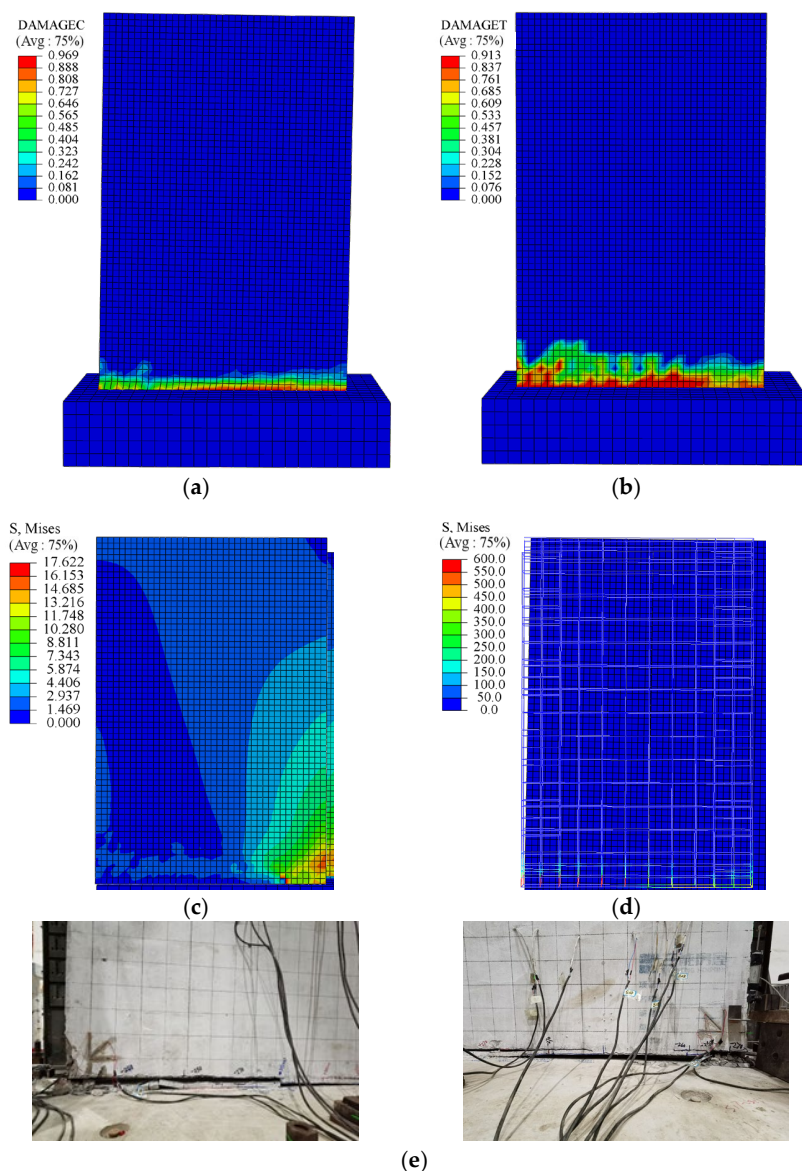


**Figure 14.** Failure models of PW1: (a) tension damage; (b) compressive damage; (c) strain of concrete (d) strain of reinforcement; and (e) actual damage in test.

### 3.4. FEA of Integral Structure

The prototype was a six-story apartment building that was designed according to the Chinese design code [44,48]. The plane layout of the building is shown in Figure 16. The main parameters of the structure were as follows: the story heights were 3 m, the length was 18 m, and the width was 13.2 m. The seismic fortification intensity was 6 degrees and the basic seismic acceleration was designed as 0.05 g. The horizontal earthquake influence coefficient was a maximum of 0.04, considering the earthquake [44]. The thickness of the wall panel was 200 mm and the thickness of the floor slab was 100 mm.

In the wall panel's integral structure, since all the members were plates, the layered shell element in ABAQUS was adopted to establish the finite element model to reduce the calculation workload and ensure convergence [49], as shown in Figure 17a. The layered shell element was divided into a concrete layer and a reinforcement layer. The reinforcement was distributed in the concrete in the form of a dispersion, and its material properties and thickness were defined. The layered shell element adopted S4R and the cell mesh size was 300 mm, which can help reduce the calculation workload with a higher accuracy. The initial axial pressure was calculated according to the actual situation of each layer.

Next, the stiffness of the nonlinear springs was set according to the alveolar-type joint constitutive model, as shown in Figure 17b. The bottom wall panels were consolidated with the foundation.

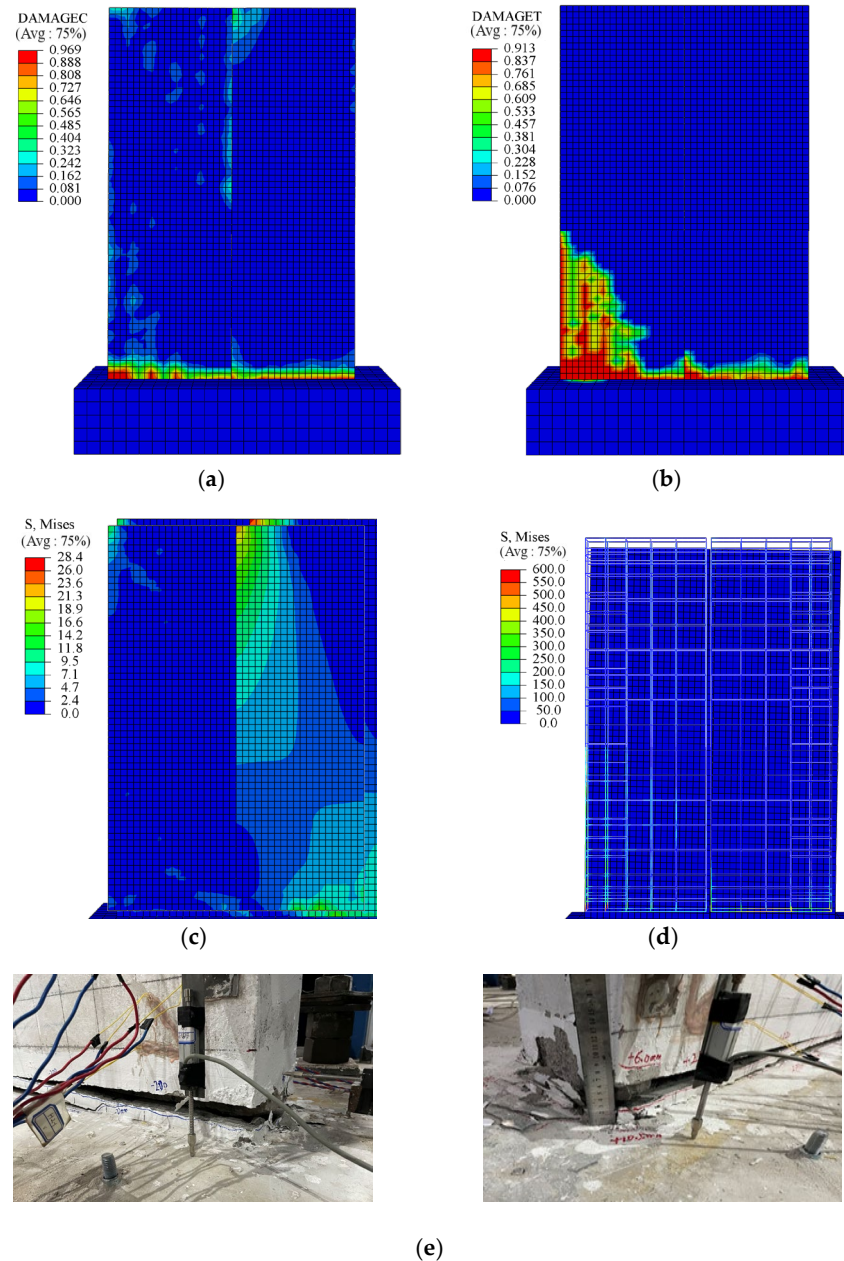


**Figure 15.** Failure models of PW2: (a) tension damage; (b) compressive damage; (c) strain of concrete (d) strain of reinforcement; and (e) actual damage in test.

Figure 18 shows the calculation results of the internal and lateral movements of the structure under both vertical and horizontal loads. It can be seen from Figure 18a that the distribution of internal forces increased from the top to the bottom under a vertical load. The connection mode can effectively realize the transmission under a vertical load. The calculation of the lateral displacement under the horizontal load is shown in Figure 18b. It can be seen that the floor's lateral displacement increased from the bottom to the top, and the maximum displacement value was 0.64 mm. Both sides of the structure before and after the lateral displacement were generally symmetrical, indicating that the stiffness distribution of the structure was relatively uniform.



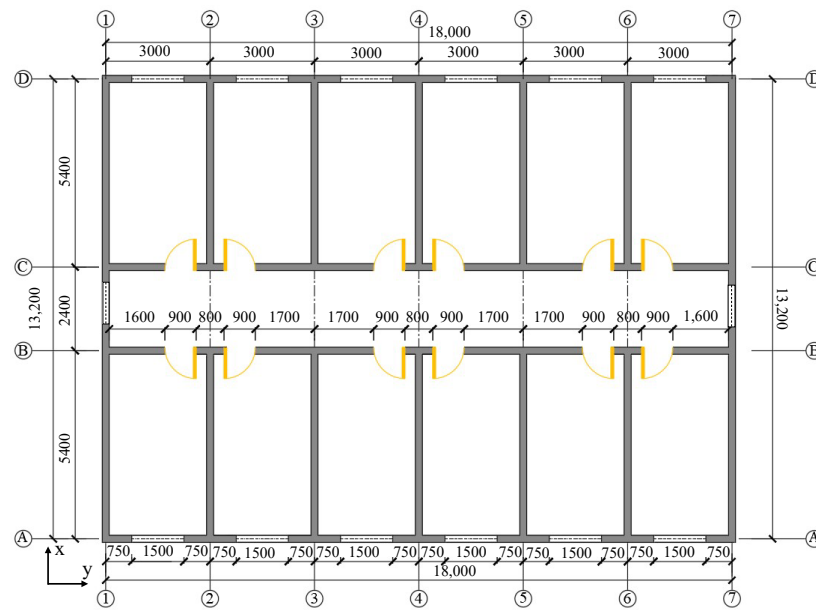


Figure 16. Prototype structure (unit: mm).

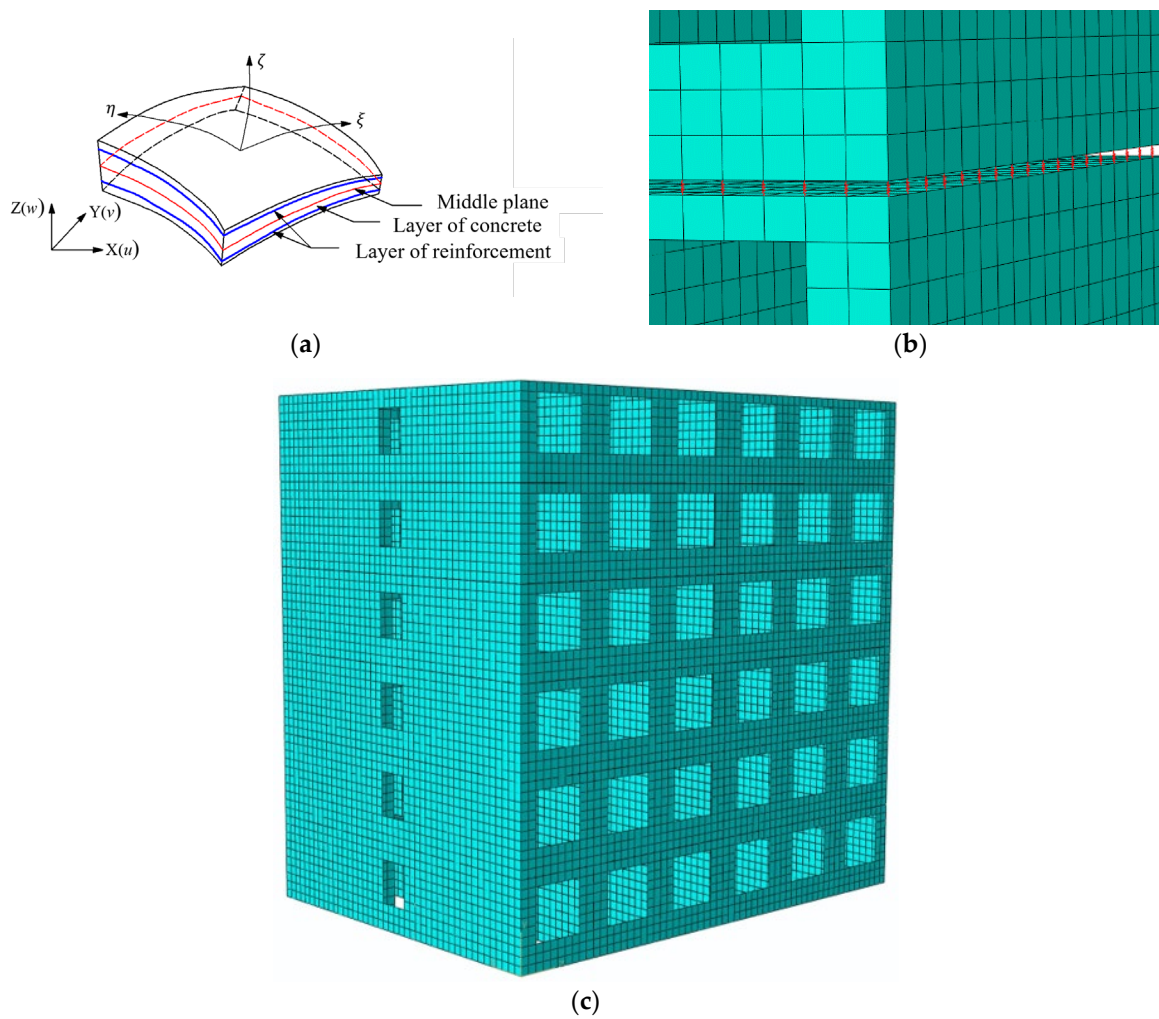


Figure 17. The FEA model of integral structure: (a) the layered shell element; (b) the nonlinear springs of the layers; and (c) the integral model.

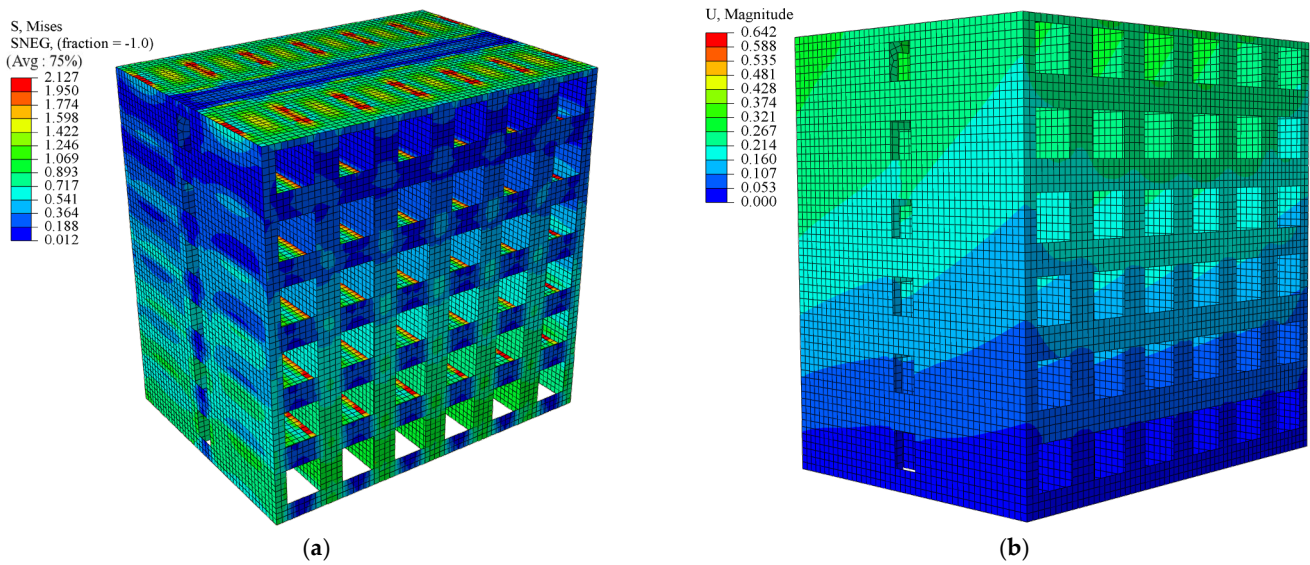


Figure 18. FEA results of integral structure: (a) internal force calculation under vertical load and (b) lateral displacement under lateral load.

#### 4. Simplified Analysis Methods of Internal Force and Verification

##### 4.1. Simplified Methods under Vertical Load

According to the exact finite element analysis results of the integral structure under the aforementioned vertical load, the force transmission path ran from the floor slab to the longitudinal and transverse wall panels, and then to the foundation. As shown in Figure 19, we can see that the load transfer to the longitudinal wall panels (the shaded green part) and the transverse wall panels (the shaded yellow part) was calculated according to the two-way plate because the side length ratio was less than three. However, the corridor floor was only supported by two sides; therefore, its load-transferring was calculated by the one-way plate. In summary, the load transmitted by the floor to the longitudinal and transverse walls can be calculated according to Equation (8) as follows:

$$\begin{aligned}
 N_x &= \frac{1}{2}(l_{x1} - \frac{1}{2}l_y)l_y \cdot q \\
 N_y &= \frac{1}{4}l_y^2 \cdot q \quad N'_y = \frac{1}{4}l_y^2 \cdot q + ql_{x2}l_y
 \end{aligned}
 \tag{8}$$

where  $N_x$  is the load transferred to longitudinal wall panels,  $N_y$  is the load transferred to transverse wall panels and  $q$  is the area load.

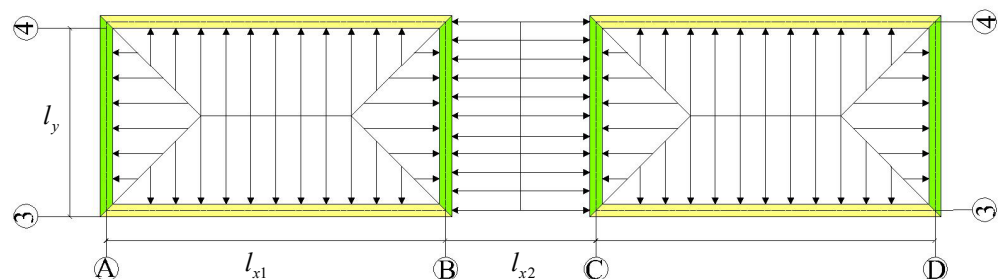


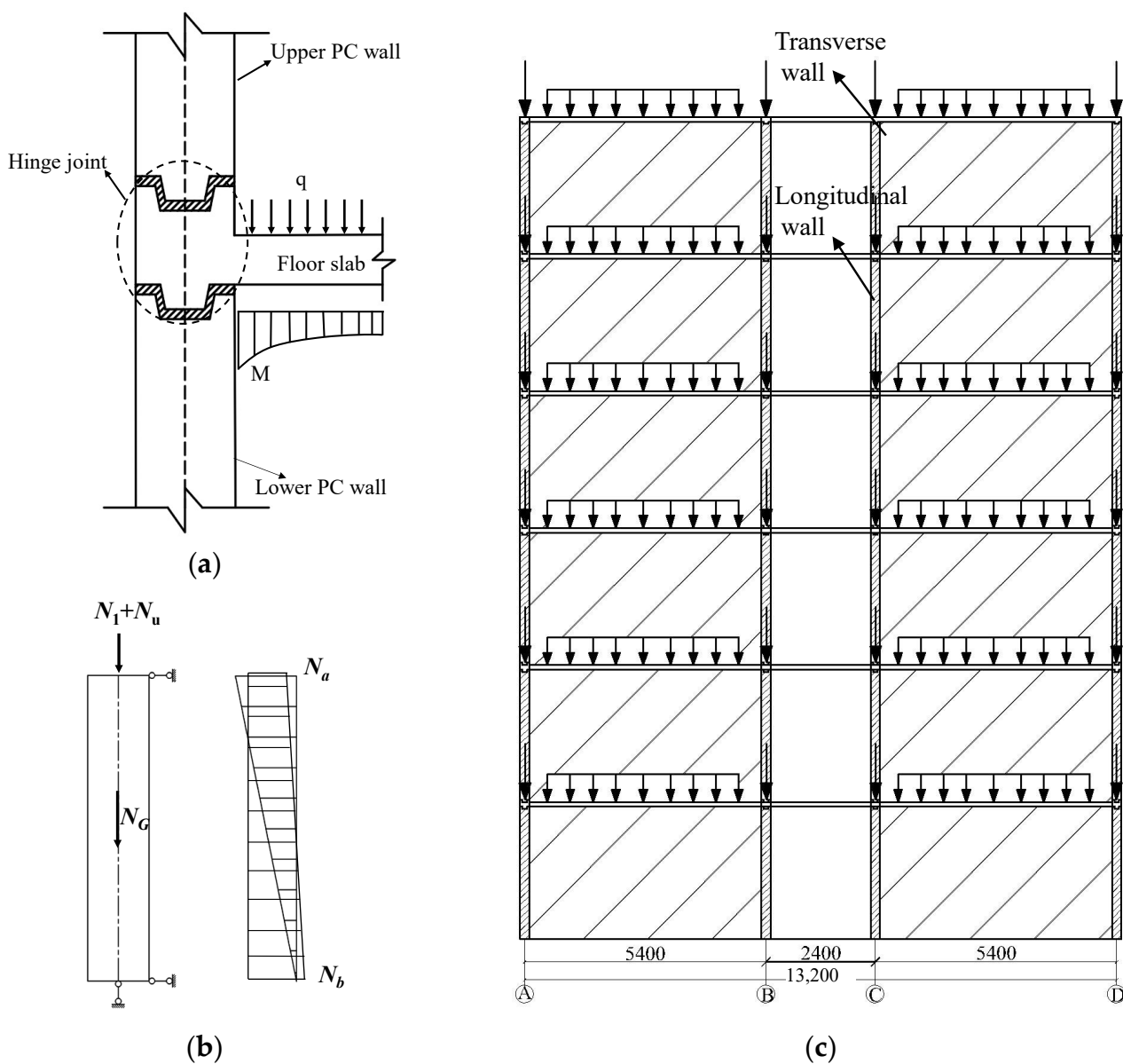
Figure 19. Schematic diagram of floor-load transferring.  $l_{x1}$  is the length of transverse wall panels,  $l_{x2}$  is the width of corridor.  $l_y$  is the length of longitudinal wall panels.

Figure 20a shows the path of the load transfer outside of the plane, where there was a positive bending moment at the joint while the load of the floor was transferred to the wall panel. It should be noted that the bending moment of the wall could be regarded as

zero, that is, the bending moment is only borne by the section of the floor. On this basis, the connection between the wall panel and the floor slab can be simplified into a hinge joint, as Figure 20b shows. Furthermore, the lateral constraint moment of the wall in the other direction was also considered. Figure 20c shows the simplified model under a vertical load. Here, we can see that only axial compression was considered, while the capacity of the wall panel against the bending moment and the shear was ignored. Equation (9) (below) produces the internal force calculation in a vertical load.

$$N_a = N_1 + N_u; \quad N_b = N_1 + N_u + N_G \quad (9)$$

where  $N_a$  are the internal forces at the upper end of the wall panel;  $N_b$  are the internal forces at the lower end of the wall panel;  $N_1$  is the load from the upper wall panel,  $N_u$  is the load from the same layer; and  $N_G$  is the self-load of the wall panel.



**Figure 20.** Simplified model under vertical load: (a) simplified hinge joint; (b) simplified model of single wall panel; and (c) integral simplified model.

#### 4.2. Simplified Methods under Lateral Load

Figure 21 shows the simplified model under a lateral load, the floor slab is simplified as a connecting rod due to its small in-plane stiffness, and the connection between the floor slab and the wall limb is simplified as a hinge joint because the constraint effect on the wall limb can be ignored. Next, each wall limb was calculated. First, the bottom horizontal load was distributed according to the stiffness of each wall limb and then it acted on them according to the original load distribution mode. Second, the internal force and lateral displacement were calculated using Equations (10) and (11) as follows:

$$V_i = \frac{K_i}{\sum_{i=1} K_i} V_0 \quad (10)$$

$$M_i = \sum F_i H_i; \quad N_i = \frac{M_i}{I} A_i y_j \quad (11)$$

where  $V_0$  is the total bottom shear;  $V_i$  is the bottom shear assigned to each wall limb;  $H_i$  is the height from the specified point to the bottom of the structure;  $A_i$  is the area of the specified section; and  $y_j$  is the distance from the specified centroid to the section centroid.

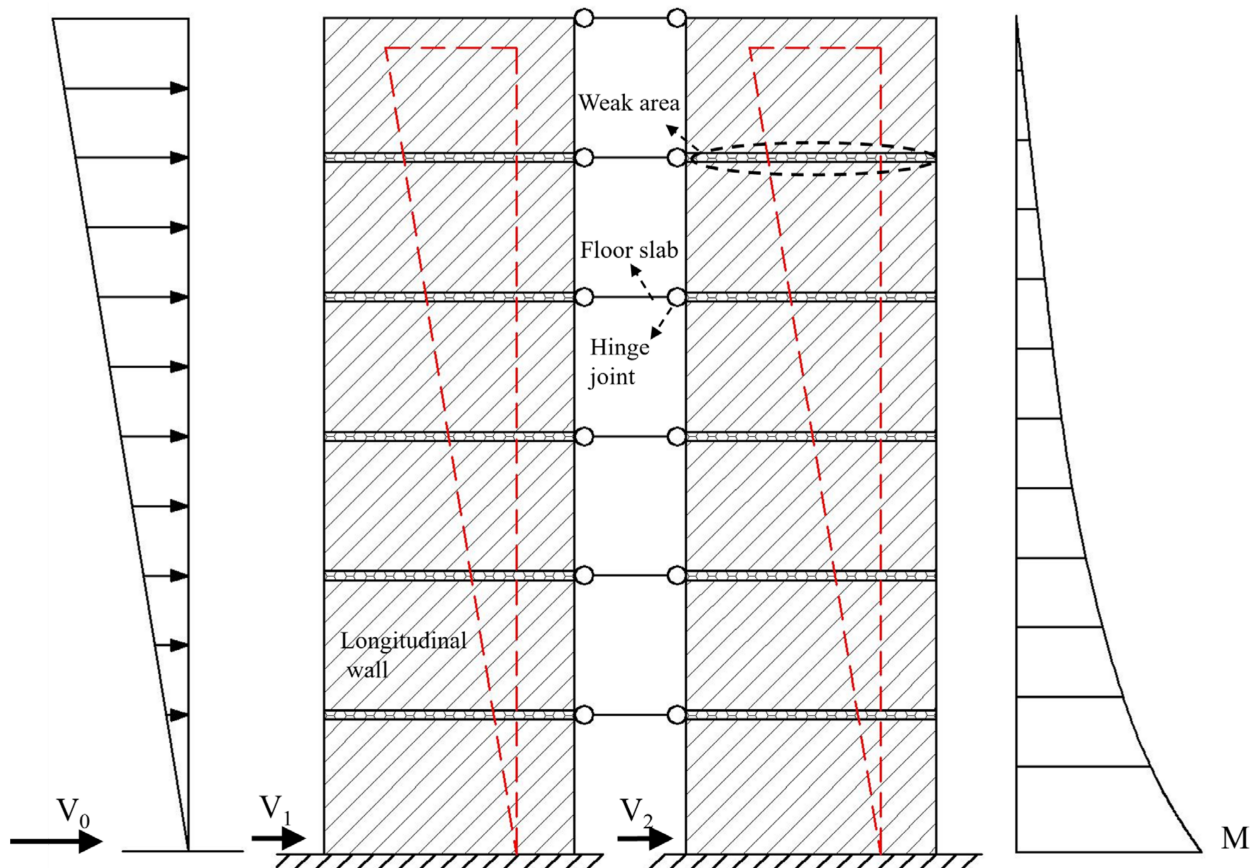


Figure 21. Simplified model under lateral load.

However, the initial elastic lateral stiffness of the wall panels was reduced due to their flexible connection with the alveolar-type joints, which should be modified. The authors of [50] studied the effects of horizontal connections, vertical connections, and reinforcement on the seismic performance of a wall constructed from a new type of assembled concrete

shear wall structure. They proposed a series of correction formulas for the elastic lateral stiffness of the wall, as shown in Equation (12) as follows:

$$K = \frac{\alpha\beta}{\gamma\left(\frac{H^3}{3E_cI_c} + \frac{\mu H}{G_cA}\right)} \quad (12)$$

where  $\alpha$  is the coefficient of the axial compression ratio and the dimension of the wall panels,  $\alpha = 2.75u^2 - 0.013\eta^2 - 0.65u + 0.043\eta + 0.28$ ;  $u$  is the axial compression ratio,  $u = N/f_cA_w$ ;  $\eta$  is the shear span ratio,  $\eta = H/b$ ;  $\beta$  is the coefficient of the horizontal joint,  $\beta = 0.9$  for the mortar joint; and  $\gamma$  is the coefficient of the reinforcement distribution,  $\gamma = 1$  for the uniformly distributed.

It should be noted that, in the above calculation, joint failure is not considered; therefore, in the case of a large load, the joint will lose bearing capacity, rendering it unable to resist the bending moment and shear force. This means that internal force redistribution will occur inside the structure; therefore, its internal force will need to be recalculated in accordance with the position and shape of the damage.

#### 4.3. Example Analysis and Verification

##### 4.3.1. Calculation and Verification under Vertical Load

Table 5 shows the different sections' axial force values, as derived from the calculations and the FEA under a vertical load. The difference between them is less than 15%, with the exception of the sixth floor. This indicates that the simplified model in the vertical load calculated the internal force of the structure accurately.

**Table 5.** Axial force of simplified model according to calculations and FEA.

Wall Panel	$\bar{N}_{i,M}$	$\bar{N}_{i,F}$	Deviation
	kN/m	kN/m	/
Top of 6F	13.51	10.29	23.9%
Bottom of 6F	30.61	38.34	20.2%
Top of 5F	48.67	50.17	3.0%
Bottom of 5F	65.77	76.12	13.6%
Top of 4F	83.83	87.73	4.5%
Bottom of 4F	100.93	113.96	11.4%
Top of 3F	118.99	125.52	5.2%
Bottom of 3F	136.09	151.78	10.3%
Top of 2F	154.15	163.33	5.6%
Bottom of 2F	171.25	190.32	10.0%
Top of 1F	189.31	201.57	6.1%
Bottom of 1F	206.41	222.37	7.2%

Note:  $\bar{N}_{i,M}$  is the unit of axial force calculated by the simplified model and  $\bar{N}_{i,F}$  is the unit of the axial force from the FEA.

##### 4.3.2. Calculation and Verification under Lateral Load

Lateral displacement under a seismic load was calculated using the aforementioned method. It should be noted that the ground wall panels were not considered in terms of stiffness reduction as they were found to be consolidated with the foundation during the finite element analysis. Table 6 shows the internal forces and displacements that were calculated between the layers. It can be seen that the finite element analysis model was in good agreement with the simplified calculation results, indicating that the simplified calculation model proposed in this paper can accurately carry out the lateral displacement of the wall panel structure under a lateral load. Figure 22 compares the displacement angles and the lateral displacement. The calculated values were slightly smaller than the results of the finite element analysis because the lateral stiffness of the floor slab was ignored; furthermore, they were both much less than the specified values under frequent earthquake conditions.

**Table 6.** Lateral displacement calculated by the FEA and simplified model.

Layer	$F_i$	$V_i$	$\Delta u_i$	$\sum_{i=1}^n \Delta u_{i,M}$	$\sum_{i=1}^n \Delta u_{i,F}$
	(kN)	(kN)	(mm)	(mm)	(mm)
6	186.0	186.0	0.037	0.518	0.486
5	164.0	350.0	0.071	0.481	0.453
4	131.0	481.0	0.100	0.409	0.364
3	98.2	579.2	0.123	0.310	0.283
2	65.5	644.7	0.153	0.187	0.162
1	32.7	677.0	0.034	0.034	0.041

Note:  $F_i$  and  $V_i$  are the earthquake force and the inter-story shear force, respectively, as calculated by the bottom shearing force method.  $\Delta u_i$  is the inter-story displacement.  $\sum_{i=1}^n \Delta u_{i,M}$  and  $\sum_{i=1}^n \Delta u_{i,F}$  are the displacement of each layer, as calculated by the simplified model and the FEA, respectively.

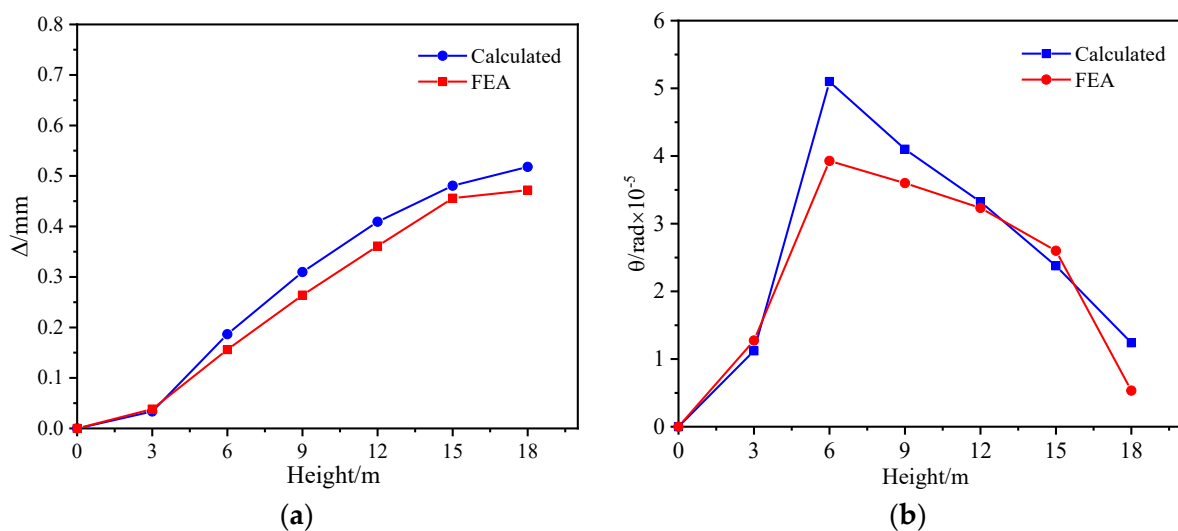


**Figure 22.** Comparison of test and FEA results under horizontal load: (a) the lateral displacement; (b) the angle of displacement between layers.

## 5. Conclusions

This paper has proposed a new prefabricated wall panel structure system based on a new connection mode that is quick to assemble and convenient. Seven monotonic load tests and two pseudo-static tests were completed, which helped to establish the shear–slip constitutive relationship of the joint interface. Corresponding finite element analysis was also conducted. On this basis, a simplified analysis model for the internal forces of the system was proposed and compared with the results of the finite element analysis. The principal conclusions can be summarized as follows:

- (1) The effects of the axial compression, mortar strength, and grouting contact area on the interface's shear resistance were investigated. It should be noted that the shear strength increased with the increase in the axial compression and mortar strength. Furthermore, the alveolar-type joint (depth 50 mm) effectively increased the grouting contact area, which increased the bearing capacity of the component by 18.6%.
- (2) The formula for the shear resistance capacity proposed in this paper agreed well with the test results, showing deviations within 10%, which suggests a certain degree of safety. On this basis, the shear–slip constitutive model was constructed by comparing the shear resistance models of different interfaces and connection forms, which was also in good agreement with the test results.
- (3) A nonlinear finite element analysis was performed using the ABAQUS program to simulate the interface and verify the reliability of the aforementioned constitutive

model. It was proven that nonlinear FEA is an accurate and effective way to evaluate the shear–slip of alveolar-type joints.

- (4) In order to facilitate internal force calculations, the simplified model under vertical and horizontal loads was established. While the axial force was approximately borne by the wall, its bending moment and shear were zero under a vertical load. However, under a horizontal load, it was equivalent to the performance of independent shear walls with weakened stiffness. The differences between the calculated results and the simulated values obtained in the example analysis were within 15%, indicating that the simplified model could approximate the internal force calculation of the system.

**Author Contributions:** Conceptualization, X.L. and Y.X.; methodology, X.L.; software, M.X.; experimental design, performance, and analysis, Y.X., M.X. and Z.P.; formal analysis, M.X.; investigation, X.L., J.C. and Y.X.; resources, Z.P.; data curation, M.X. and J.C.; writing—original draft preparation, Y.X.; writing—review and editing, Y.X., M.X. and J.L.; visualization, J.L. and Z.P.; supervision, X.L.; project administration, X.L.; funding acquisition, X.L. All authors have read and agreed to the published version of the manuscript.

**Funding:** This research was funded by the National Natural Science Foundation of China (Grant No. 52178179).

**Data Availability Statement:** The data presented in this study are available on request from the corresponding author.

**Conflicts of Interest:** The authors declare no conflict of interest.

## References

1. Alfred, A.Y. Social and Environmental Benefits of Precast Concrete Technology. *PCI J.* **2001**, *46*, 14–19. [[CrossRef](#)]
2. Cheng, J.; Luo, X.; Cheng, L.; Cheng, Q.; Chen, L. Experimental Study on Seismic Behavior of PC Walls with Alveolar-Type Horizontal Joint under Pseudo-Static Loading. *Materials* **2022**, *15*, 2301. [[CrossRef](#)] [[PubMed](#)]
3. Guo, W.; Zhai, Z.; Cui, Y.; Yu, Z.; Wu, X. Seismic performance assessment of low-rise precast wall panel structure with bolt connections. *Eng. Struct.* **2019**, *181*, 562–578. [[CrossRef](#)]
4. Xu, G.; Wang, Z.; Wu, B.; Bursi, O.S.; Tan, X.; Yang, Q.; Wen, L. Seismic performance of precast shear wall with sleeves connection based on experimental and numerical studies. *Eng. Struct.* **2017**, *150*, 346–358. [[CrossRef](#)]
5. Mochizuki, S.; Kobayashi, T. Experiment on slip strength of horizontal joint of precast concrete multi-story shear wall. *J. Struct. Constr. Eng.* **1996**, *194*, 1–8.
6. Bhatt, P. Influence of vertical joints on the behavior of precast shear walls. *Build. Sci.* **1973**, *8*, 221–224. [[CrossRef](#)]
7. Ling, J.H.; Abd Rahman, A.B.; Ibrahim, I.S.; Abdul Hamid, Z. Behavior of grouted pipe splice under incremental tensile load. *Constr. Build. Mater.* **2012**, *33*, 90–98. [[CrossRef](#)]
8. Belleri, A.; Riva, P. Seismic performance and retrofit of precast concrete grouted sleeve connections. *PCI J.* **2012**, *57*, 97–109. [[CrossRef](#)]
9. Zhang, Z.; Zheng, G. Seismic performance of the spatial model of precast concrete shear wall structure using grouted lap splice connection and cast-in-situ concrete. *Struct. Concr.* **2019**, *20*, 1316–1327. [[CrossRef](#)]
10. Zhou, Y.; Zhang, B.; Hwang, H.; Xi, S.; Fang, L.; Huang, Y.; Yi, W. Tensile and shear behavior of box connector for precast concrete shear walls. *Eng. Struct.* **2021**, *245*, 112983. [[CrossRef](#)]
11. Kurama, Y.; Pessiki, S.; Sause, R.; Le-Wu, L. Seismic Behavior and Design of unbonded post-tensioned precast concrete walls. *PCI J.* **1999**, *44*, 72–89. [[CrossRef](#)]
12. Hutchinson, R.L.; Rizkalla, S.H.; Lau, M.; Heuvel, S. Horizontal Post-Tensioned Connections for Precast Concrete Load bearing Shear Wall Panels. *PCI J.* **1991**, *36*, 64–76. [[CrossRef](#)]
13. Xiao, X.; Cao, Z.; Liu, X.; Liao, X. Experimental study on seismic performance of precast shear wall with unconnected vertical distributed reinforcement. *Build. Struct.* **2021**, *51*, 5–9. [[CrossRef](#)]
14. Ying, J. Investigation on applicable and physical properties of prefabricated large panel housing. *Urban Probl.* **2011**, *191*, 37–42. [[CrossRef](#)]
15. Jiang, Q.; Shen, J.; Chong, X.; Chen, M.; Wang, H.; Feng, Y.; Huang, J. Experimental and numerical studies on the seismic performance of superimposed reinforced concrete shear walls with insulation. *Eng. Struct.* **2021**, *240*, 112372. [[CrossRef](#)]
16. Zhang, D.; Huang, B.; Zhang, Y.; Yu, S.; Bie, J. Theoretical Study and Nonlinear Finite Analysis of Four-Line Restoring Force Model for Double-Superimposed Slab Shear Walls. *Buildings* **2023**, *13*, 749. [[CrossRef](#)]

17. Chong, X.; Xie, L.; Ye, X.; Jiang, Q.; Wang, D. Experimental Study on the Seismic Performance of Superimposed RC Shear Walls with Enhanced Horizontal Joints. *JEE* **2019**, *23*, 1–17. [[CrossRef](#)]
18. Hong, Z.; Xi, L. Nonlinear behavior of partially prefabricated reinforced concrete composite walls. *China Civ. Eng. J.* **2010**, *43*, 93–100. [[CrossRef](#)]
19. Yu, G.; Xin, W. Application and development of a new type of wall material-Rapid wall panel. *Sichuan J. Archit.* **2008**, *28*, 196–197.
20. Zhang, X.; Wang, Y.; Lu, Z.; Yuan, Y. Experimental study on seismic performance of shear wall with precast concrete hollow molds. *Struct. Concr.* **2021**, *22*, 1445–1461. [[CrossRef](#)]
21. Chu, M.; Xiong, C.; Liu, J.; Sun, Z. Experimental study on shear behavior of two-way hollow core precast panel shear wall with vertical connection. *Struct. Des. Tall Spec. Build.* **2021**, *30*, e1814. [[CrossRef](#)]
22. Li, Y.; Li, Z.; Tang, Z.; Xu, L.; Wang, W.; Yang, X.; Chen, Y. Cyclic behavior of hollow-core precast shear walls subjected to different axial loads. *Eng. Struct.* **2023**, *276*, 115343. [[CrossRef](#)]
23. Wang, W.; Wang, X. Experimental and numerical investigations on concentrated-hollow RC shear walls. *Eng. Struct.* **2021**, *242*, 112570. [[CrossRef](#)]
24. Ravasini, S.; Belletti, B.; Brunesi, E.; Nascimbene, R.; Parisi, F. Nonlinear Dynamic Response of a Precast Concrete Building to Sudden Column Removal. *Appl. Sci.* **2021**, *11*, 599. [[CrossRef](#)]
25. Khaled, A.; Soudki, J.S.; West, S.H.; Rizkalla, B.B. Horizontal Connections for Precast Concrete Shear Wall Panels Under Cyclic Shear Loading. *PCI J.* **1996**, *41*, 64–80. [[CrossRef](#)]
26. Xi, Z.; Jian, M.; Peng, H. Shear behavior on prefabricated shear wall alveolar type connection. *J. Build. Struct.* **2017**, *38*, 93–100. [[CrossRef](#)]
27. GB/T 50081-2019; Standard Test Method for Physical and Mechanical Properties of Concrete. China Architecture & Building Press: Beijing, China, 2019.
28. JGJ/T 101-2015; Specification for Seismic Test of Buildings. China Architecture & Building Press: Beijing, China, 2015.
29. Randle, N. Design recommendations for interface shear transfer in fib Model Code 2010. *Struct. Concr.* **2013**, *14*, 230–241. [[CrossRef](#)]
30. Pramodh, R.; Shripriyadharshini, V.; Vidjeapriya, R. Shear behavior of horizontal joints between precast panels. *Asian J. Civ. Eng.* **2018**, *19*, 651–662. [[CrossRef](#)]
31. GB/T 51231-2016; Technical Standard for Assembled Buildings with Concrete Structure. Architecture & Building Press: Beijing, China, 2016.
32. International Federation for Structure Concrete. *fib Model Code for Concrete Structures 2010*; Ernst & Sohn: Berlin, Germany, 2013; pp. I–XXXIII. [[CrossRef](#)]
33. Mattock, A.H.; Hawkins, N.M. Shear Transfer in Reinforced Concrete—Recent Research. *J. Prestress. Concr. Inst.* **1972**, *17*, 55–75. [[CrossRef](#)]
34. Yong, Z.; Yu, W.; Xiao, W. Experimental study on shear performance of steel sleeve grouting joint. *J. Build. Struct.* **2021**, *42*, 221–230. [[CrossRef](#)]
35. Yong, Z.; Ren, Z. *Experimental Investigation on Interface of High Strength Concretes Cast at Different Times under Direct Shear*; College of Civil Engineering, Tongji University: Shanghai, China, 2017; Volume 45, pp. 962–969.
36. Zhao, F.; Xiong, F.; Cai, G.; Yan, H.; Liu, Y.; Si Larbi, A. Performance and numerical modelling of full-scale demountable bolted PC wall panels subjected to cyclic loading. *J. Build. Eng.* **2023**, *63*, 105556. [[CrossRef](#)]
37. Chen, W.; Wu, Q.; Wu, D.; Dang, L.; Jiang, F. Numerical Theoretical Study on Mechanical Properties of New Reinforced Tenon Precast Shear Walls. *Adv. Civ. Eng.* **2020**, *2020*, 3784271. [[CrossRef](#)]
38. Li, J.; Wang, Y.; Lu, Z.; Li, J. Experimental Study and Numerical Simulation of a Laminated Reinforced Concrete Shear Wall with a Vertical Seam. *Appl. Sci.* **2017**, *7*, 629. [[CrossRef](#)]
39. Sun, J.; Qiu, H.; Lu, Y. Experimental study and associated numerical simulation of horizontally connected precast shear wall assembly. *Struct. Design Tall Spec. Build.* **2016**, *25*, 659–678. [[CrossRef](#)]
40. Xu, W.; Yang, X.; Wang, F.; Chi, B. Experimental and Numerical Study on the Seismic Performance of Prefabricated Reinforced Masonry Shear Walls. *Appl. Sci.* **2018**, *8*, 1856. [[CrossRef](#)]
41. Halahla, A.M.; Rahman, M.K.; Al-Gadhib, A.H.; Al-Osta, M.A.; Baluch, M.H. Experimental investigations and FE simulation of exterior BCJs retrofitted with CFRP fabric. *Earthq. Struct.* **2019**, *17*, 337–354. [[CrossRef](#)]
42. ABAQUS, 6.13.1; Dassault Systemes Simulia: Providence, RI, USA, 2013.
43. Naser, M.Z.; Hawileh, R.A.; Abdalla, J. Modeling Strategies of Finite Element Simulation of Reinforced Concrete Beams Strengthened with FRP: A Review. *J. Compos. Sci.* **2021**, *5*, 19. [[CrossRef](#)]
44. GB/T 50010-2010; Code for Design of Concrete Structures. China Architecture & Building Press: Beijing, China, 2010.
45. Lubliner, J.; Oliver, J.; Oller, S.; Oñate, E. A Plastic-Damage Model for Concrete. *Int. J. Solids Struct.* **1989**, *25*, 299–326. [[CrossRef](#)]
46. Lee, J.; Fenves, G.L. Plastic-damage model for cyclic loading of concrete structures. *J. Eng. Mech.* **1998**, *124*, 892–900. [[CrossRef](#)]
47. Ming, X.; Yuan, H.; Rui, Z. Seismic analysis of precast concrete shear wall with horizontal seam. *Earthq. Eng. Eng. Dyn.* **2014**, *34*, 95–104. [[CrossRef](#)]
48. GB/T 50011-2010; Code for Seismic Design of Buildings. China Architecture & Building Press: Beijing, China, 2010.



49. Xiang, Z.; Yuan, L.; Guo, Z.; Min, Y.; Tan, W. Analysis of seismic performance simulation of precast shear wall based on multi-layer shell elements. *Eng. J. Wuhan Univ.* **2022**, *55*, 45–53. [[CrossRef](#)]
50. Wei, H.; Bin, L.; Yan, S.; Yun, Z.; Yong, J. Study on restoring force model of new precast seismic walls. *Earthq. Eng. Eng. Dyn.* **2017**, *37*, 123–134. [[CrossRef](#)]

**Disclaimer/Publisher’s Note:** The statements, opinions and data contained in all publications are solely those of the individual author(s) and contributor(s) and not of MDPI and/or the editor(s). MDPI and/or the editor(s) disclaim responsibility for any injury to people or property resulting from any ideas, methods, instructions or products referred to in the content.